Bulletin of Mathematical Biology (2020) 82:30
https://doi.org/10.1007/s11538-020-00703-4

Society for Mathematical Biology

ORIGINAL ARTICLE

Stability Analysis of a Bulk–Surface Reaction Model for Membrane Protein Clustering

Lucas M. Stolerman[1] · Michael Getz[1] · Stefan G. Llewellyn Smith[1,2] · Michael Holst[3,4] · Padmini Rangamani[1]

Received: 14 August 2019 / Accepted: 22 January 2020 / Published online: 6 February 2020
© Society for Mathematical Biology 2020

Abstract

Protein aggregation on the plasma membrane (PM) is of critical importance to many cellular processes such as cell adhesion, endocytosis, fibrillar conformation, and vesicle transport. Lateral diffusion of protein aggregates or clusters on the surface of the PM plays an important role in governing their heterogeneous surface distribution. However, the stability behavior of the surface distribution of protein aggregates remains poorly understood. Therefore, understanding the spatial patterns that can emerge on the PM solely through protein–protein interaction, lateral diffusion, and feedback is an important step toward a complete description of the mechanisms behind protein clustering on the cell surface. In this work, we investigate the pattern formation of a reaction–diffusion model that describes the dynamics of a system of ligand–receptor complexes. The purely diffusive ligand in the cytosol can bind receptors in the PM and the resultant ligand–receptor complexes not only diffuse laterally but can also form clusters resulting in different oligomers. Finally, the largest oligomers recruit ligands from the cytosol using positive feedback. From a methodological viewpoint, we provide theoretical estimates for diffusion-driven instabilities of the protein aggregates based on the Turing mechanism. Our main result is a threshold phenomenon, in which a sufficiently high recruitment of ligands promotes the input of new monomeric components and consequently drives the formation of a single-patch spatially heterogeneous steady state.

Keywords Plasma membrane · Membrane protein clustering · Bulk–surface models · Surface diffusion · Geometric PDE · Stability analysis

L. M. Stolerman and M. Getz have contributed equally to this work.

Electronic supplementary material The online version of this article (https://doi.org/10.1007/s11538-020-00703-4) contains supplementary material, which is available to authorized users.

✉ Padmini Rangamani
prangamani@ucsd.edu

Extended author information available on the last page of the article

1 Introduction

Biological membranes are unique two-dimensional structures that separate cellular contents from the extracellular environment and regulate the transport of material into and out of the cell (Darnell et al. 1990; Stillwell 2013). In addition to lipids and carbohydrates, these membranes contain a large proportion of proteins, the composition of which depends on the cell type (Stillwell 2013; Guidotti 1972; Yeagle 2011; Albersheim and Anderson-Prouty 1975; Jain and Wagner 1988). One of the interesting features of membrane proteins is their ability to form clusters on the cell surface (Hashimoto and Panchenko 2010; Johannes et al. 2018; Ispolatov 2005). This clustering of proteins on the plasma membrane (PM) results in a spatial heterogeneity in the distribution of protein densities. Many factors can induce such a spatial heterogeneity, including lateral diffusion, physical barriers from the cytoskeleton (Porat-Shliom et al. 2013), lipid raft affinity (Lorent et al. 2017), and curvature differences along the membrane (Johannes et al. 2018). The formation of protein clusters is intimately related to various cellular phenomena such as polarization, membrane depolarization, receptor signaling, enzyme activity, and cytoskeletal regulation (Mori et al. 2008; Lao et al. 2010; Lemmon and Schlessinger 2010; Sleno and Hbert 2018; Baisamy et al. 2005; Chen et al. 2005).

A particular example of proteins forming clusters on the membrane is well elucidated by amyloid-β aggregation/fibrillation in the context of Alzheimer's disease. It is thought that amyloid-β can become cytotoxic when it aggregates on the membrane at high levels (Askarova et al. 2011). Biophysical measurements show that amyloid-β aggregates become more stable when oligomerized (i.e., when it forms molecular components from repeating units) on the membrane surface (Sarkar et al. 2013; Zhang et al. 2012) and can also destabilize certain membrane compositions (Andreasen et al. 2015). It is also thought that membrane components such as cholesterol may initiate aggregation of amyloid-β, which may then be bolstered by a yet unidentified secondary feedback mechanism (Habchi et al. 2018). In general, the aggregation of proteins on the membrane surface appears to be a common mechanism for fibrillar protein aggregation and aggregate propagation in a variety of neurodegenerative diseases (Holmes and Diamond 2012; Rawat et al. 2018). In addition to amyloid-β, surface receptors such as α-amino-3-hydroxy-5-methyl-4-isoxazolepropionic acid receptor (AMPAR) (Choquet 2010; Gan et al. 2015) and membrane-bound kinases such as Fyn (Padmanabhan et al. 2019) are known to cluster on the membrane; these clusters have been implicated in neuronal functioning in physiology (Lorent et al. 2017; Lao et al. 2010) and disease (Askarova et al. 2011; Andreasen et al. 2015).

One of the open questions in the field of protein aggregations is the role of the spatial organization of membrane proteins due to bulk–surface reactions and feedback mechanisms. Mathematical modeling has provided substantial insight into the geometric coupling of bulk–surface reaction–diffusion systems (Rangamani et al. 2013; Frey et al. 2018; Denk et al. 2018), including wave-pinning formulations (Mori et al. 2008; Cusseddu et al. 2018), spatial patterning (Giese et al. 2015; Diegmiller et al. 2018), and generalized stability analysis (Madzvamuse et al. 2015; Rätz and Röger 2012; Rätz 2015). From a modeling perspective, several authors have proposed the classical Smoluchowski coagulation model (Smoluchowski 1918; Drake 1972) as a

suitable candidate for describing protein aggregation. The system of differential equations in the Smoluchowski model deserves attention as it accounts for the changes in concentration of interacting molecules with different sizes. These molecules can thus reversibly aggregate according to a given *aggregation kernel*. In the recent past, the use of such kernels (Arosio et al. 2012; Zidar et al. 2018) allowed for a successful combination of experimental measurements with computational predictions. These models performed well in terms of comparisons to data and estimation of kinetic parameters such as the aggregation time and the asymptotic cluster distribution. However, by using the original Smoluchowski systems of ordinary differential equations (ODEs), these studies lack descriptions of the spatial protein organization, which can be crucial for the understanding of many cellular processes. To overcome this limitation, one can explicitly consider molecular diffusion and use systems of partial differential equations (PDEs), as has been done in the amyloid-β aggregation models (Achdou et al. 2013; Franchi and Lorenzani 2016; Bertsch et al. 2016). These studies have provided detailed theoretical estimates in terms of boundary conditions and homogenization tools. However, they have restricted the spatial scale to a small three-dimensional region of cerebral tissue and do not describe intracellular phenomena. There is thus a need for mathematical models of protein aggregation in the PM with proper spatial description to account for the numerous cellular processes that occur due to heterogeneous protein distribution.

In this work, our primary goal was to investigate the emergence of spatially heterogeneous steady-state profiles of membrane protein aggregates to identify how feedback between cytosolic and membrane components can drive pattern formation on the membrane. To this end, we merged the concept of bulk–surface reaction–diffusion systems with the Smoluchowski approach to introduce a new bulk–surface model for membrane protein clustering (Fig. 1a). The model equations describe a purely diffusive ligand in the cytosol, which then undergoes membrane binding without any cytosolic aggregation. The resultant membrane-bound protein can diffuse laterally and also form clusters with different oligomeric sizes. Finally, the oligomers of maximum size can further recruit more cytosolic proteins, resulting in a positive feedback for the membrane protein aggregates and stabilization of the oligomers (Habchi et al. 2018; Sarkar et al. 2013). Following the approach of Rätz and Röger (2012), Rätz (2015), we then analyzed the model for diffusion-driven instabilities using the classical Turing mechanisms. We found these interactions allow diffusion-driven instabilities and pattern formation in the absence of a sustained localized stimulus.

In what follows, we present the model assumptions and derivation in Sect. 2 and the mathematical analysis including stability analysis in Sect. 3 and conclude with numerical simulations (Sect. 4) and a discussion (Sect. 5) about our findings in the context of amyloid-β and clustering of other membrane proteins.

2 Model Development

Here we present our bulk–surface reaction–diffusion model for protein aggregation, including feedback. We describe our assumptions (Sect. 2.1) and the governing equations (Sect. 2.2) in detail. In Sect. 2.3, we prove that the total mass of the system

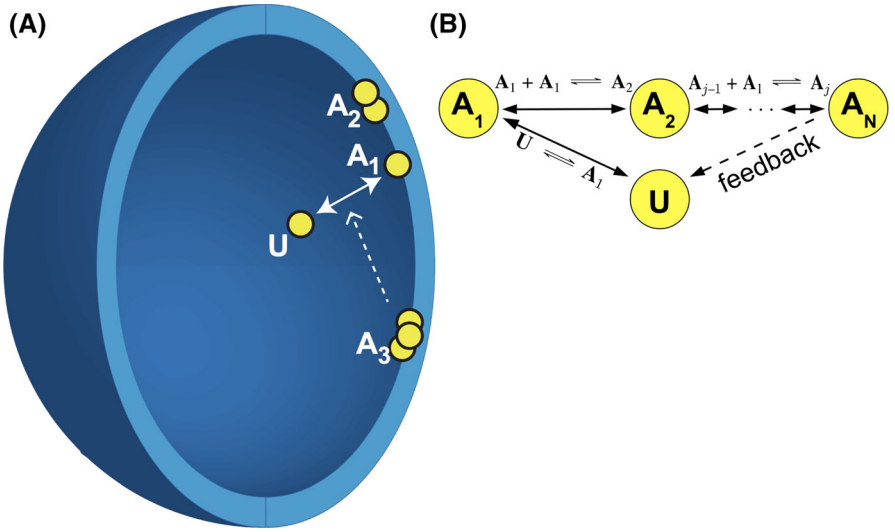

Fig. 1 A bulk–surface compartmental model for protein aggregation. **a** As proteins approach the surface, they can associate and then oligomerize. This oligomerization then drives further membrane association of monomers. In this figure, we assume that the maximum oligomer size is three and the arrows represent a state change of $\mathbf{U}$ to $\mathbf{A}_1$; the dotted line shows the "catalytic" feedback of $\mathbf{A}_3$ to $\mathbf{U}$ and $\mathbf{A}_1$. **b** A detailed diagram of all chemical reactions for an arbitrary maximum oligomer size N (Color figure online)

is conserved over time, and in Sect. 2.4, we non-dimensionalize the model. Finally, in section Sect. 2.5, we perform the system's reduction when the cytosolic diffusion goes to infinity, following the mathematical approach of Rätz and Röger (2012), Rätz (2015).

2.1 Assumptions

In our system, we assume that $\mathbf{U}$ represents the volume component, which can freely diffuse in the cytoplasm. Upon binding to the plasma membrane, it forms a surface monomer component $\mathbf{A}_1$. The $\mathbf{A}_1$ molecules laterally diffuse in the membrane and form the oligomeric components $\mathbf{A}_j$. Here, j denotes the number of $\mathbf{A}_1$ molecules in the oligomer, which is at most $N \in \mathbb{N}$. In terms of chemical reactions, $\mathbf{U} \overset{f}{\rightleftharpoons} \mathbf{A}_1$ denotes the binding of the cytosolic component to the plasma membrane with a reaction flux f. The subsequent oligomerization at the membrane is described by

$$\mathbf{A}_{j-1} + \mathbf{A}_1 \rightleftharpoons \mathbf{A}_j \quad \text{for} \quad j = 2, 3, \ldots, N.$$

We also assume that the flux term f describes ligand binding/unbinding to the cell surface, where the binding term will be linearly proportional to the concentrations of $\mathbf{U}$ in the cytosol and $\mathbf{A}_N$ in the plasma membrane. In Fig. 1b, we illustrate the reactions taking place in our system: the exchange between cytosolic and membrane-bound monomer, the formation of dimers, the general oligomerization reactions, and the

positive feedback. The oligomerization process is modeled as a particular version of the reversible Smoluchowski model for aggregation dynamics (Bentz and Nir 1981). We also assume that the oligomerization process occurs only by monomer attachment in the mass action regime. Moreover, to keep the analysis tractable, we do not consider any cooperativity term such as Hill's function (Changeux et al. 1967): the rate at which different oligomers are formed is independent of their size.

2.2 Governing Equations

We represent the cellular domain as the bounded region Ω with smooth boundary $\Gamma = \partial\Omega$. We define the concentrations $u(x,t) : \Omega \times (0,\mathcal{T}] \to \mathbb{R}$ for the volume component and $a_j(x,t) : \Gamma \times (0,\mathcal{T}] \to \mathbb{R}$ for the membrane oligomeric components, where x and t represent the location and time, respectively. The molecular mechanisms underlying membrane protein aggregation and stabilization are quite complex. However, from a feedback standpoint, the so-called rich gets richer phenomenon seems to be prevalent in various systems, especially in the context of amyloid fibrillation (Chatani and Yamamoto 2018; Crespo et al. 2012; Johnson et al. 2012; Jarrett and Lansbury 1993; Cohen et al. 2012; Arosio et al. 2015; Meisl et al. 2016). Therefore, we propose a mathematically tractable *feedback term* to represent this complex mechanism. The flux term is thus defined as

$$f(u, a_1, a_N) = (k_0 + k_b a_N)u - k_d a_1 \tag{1}$$

for k_0, k_b, and k_d positive constants, where k_0 is the basal binding rate, k_b is the rate of A_N-dependent binding rate, and k_d is the unbinding rate from the membrane into the cytosol. Then, the governing equations for the spatiotemporal evolution of different components are given by

$$\partial_t u = D_u \nabla^2 u \tag{2}$$

$$\begin{aligned}\partial_t a_1 = {} & D_1 \Delta a_1 + (k_0 + k_b a_N)u - k_d a_1 - 2k_m a_1^2 + 2k_2 a_2 \\ & - k_g a_1 \left(\sum_{l=2}^{N-1} a_l \right) + \sum_{j=3}^{N} k_j a_j \end{aligned} \tag{3}$$

$$\partial_t a_2 = D_2 \Delta a_2 + k_m a_1^2 - k_g a_1 a_2 - k_2 a_2 + k_3 a_3 \tag{4}$$

$$\partial_t a_j = D_j \Delta a_j + k_g a_1 a_{j-1} - k_g a_1 a_j - k_j a_j + k_{j+1} a_{j+1}, \quad j = 3, \ldots, N-1 \tag{5}$$

$$\partial_t a_N = D_N \Delta a_N + k_g a_1 a_{N-1} - k_N a_N. \tag{6}$$

Here, ∇^2 and Δ represent the Laplace and Laplace–Beltrami operators, respectively. The parameter k_m represents the rate at which monomers bind to form dimers. The rate k_g at which the oligomers of size greater than two are formed is assumed to be the same for all oligomerization reactions. Finally, k_j represent the rates at which the oligomeric components of size j will release a single monomer. The boundary

condition for a is periodic since the domain is closed and the boundary condition for u is given by

$$-D_u\,(\mathbf{n}\cdot\nabla u)\Big|_{x\in\Gamma} = (k_0 + k_b a_N)u - k_d a_1 \tag{7}$$

as a balance of the diffusive flux and the reaction rate at the membrane. All parameters and variables are nonnegative real numbers.

2.3 Mass Conservation

Let n_X denote the number of molecules of the component X. For a closed system, we know that the total number of single molecules must be given by

$$n_U + n_{A_1} + 2n_{A_2} + \ldots + Nn_{A_N}$$

since each A_j oligomer must have exactly j molecules of A_1. From this fact, we define the total mass of the system, which accounts for spatial compartments (bulk and surface) and different molecular size distributions. This is the content of the following

Proposition 2.1 *Let $u, a_1, a_2, \ldots, a_N$ be solutions of (2)–(7). Then, the quantity*

$$M(t) := \int_\Omega u(x,t)dx + \sum_{j=1}^{N}\left\{ j\cdot\int_\Gamma a_j(x,t)ds\right\} \tag{8}$$

represents the total mass of the system and is conserved over time, i.e., $M(t) = M_0 \;\; \forall t \geq 0$. In this case, M_0 denotes the initial mass which is given by $M_0 = \int_\Omega u(x,0)dx + \sum_{j=1}^{N}\left\{ j\cdot\int_\Gamma a_j(x,0)ds\right\}$

Proof By taking the time derivative of $M(t)$ and assuming u and a_j are $\mathcal{C}^2$ solutions for (2)–(7), we have

$$\frac{\mathrm{d}}{\mathrm{d}t}M = \int_\Omega \partial_t u\,\mathrm{d}x + \sum_{j=1}^{N}\left\{ j\cdot\int_\Gamma \partial_t a_j\,\mathrm{d}s\right\}.$$

For the integral $\int_\Omega \partial_t u\mathrm{d}x$, we apply the divergence theorem and substitute Eq. (7) to obtain

$$\begin{aligned}\int_\Omega \partial_t u\mathrm{d}x &= D_u\int_\Omega \nabla^2 u\mathrm{d}x\\ &= D_u\int_\Gamma (\nabla u\cdot\mathbf{n})\mathrm{d}s\\ &= -\int_\Gamma [(k_0+k_b a_N)u - k_d a_1]\mathrm{d}s.\end{aligned}$$

For the summation of surface integrals $\sum_{j=1}^{N}\left\{j\cdot\int_\Gamma \partial_t a_j \mathrm{d}s\right\}$, we substitute the governing equations to obtain

$$\begin{aligned}
\sum_{j=1}^{N}\left\{j\cdot\int_\Gamma \partial_t a_j \mathrm{d}s\right\} &= \int_\Gamma \Big[D_1\Delta a_1 + (k_0+k_b a_N)u - k_d a_1 - 2k_m a_1^2 + 2k_2 a_2 \\
&\quad -k_g a_1\left(\sum_{l=2}^{N-1} a_l\right) + \sum_{j=3}^{N} k_j a_j\Big]\mathrm{d}s \\
&\quad + \int_\Gamma \Big[2\cdot D_2\Delta a_2 + 2\cdot\left\{k_m a_1^2 - k_g a_1 a_2 - k_2 a_2 + k_3 a_3\right\}\Big]\mathrm{d}s \\
&\quad + \sum_{j=3}^{N-1}\int_\Gamma \Big[j\cdot D_j\Delta a_j + j\cdot\left\{k_g a_1 a_{j-1} - k_g a_1 a_j - k_j a_j + k_{j+1}a_{j+1}\right\}\Big]\mathrm{d}s \\
&\quad + \int_\Gamma N\cdot\left[D_N\Delta a_N\right] + N\cdot\left\{k_g a_1 a_{N-1} - k_N a_N\right\}\Big]\mathrm{d}s \\
&= \sum_{j=1}^{N} j D_j\cdot\int_\Gamma \Delta a_j \mathrm{d}s + \int_\Gamma (k_0+k_b a_N)u - k_d a_1 \mathrm{d}s \\
&= \int_\Gamma \left((k_0+k_b a_N)u - k_d a_1\right)\mathrm{d}s
\end{aligned}$$

where the last equality comes from the fact that $\int_\Gamma \Delta a_j \mathrm{d}s = 0$ as a consequence of the first Green's theorem (van Oosterom 2006). We therefore have

$$\frac{\mathrm{d}}{\mathrm{d}t}M = \int_\Omega \partial_t u \mathrm{d}x + \sum_{j=1}^{N}\left\{j\cdot\int_\Gamma \partial_t a_j \mathrm{d}s\right\} = 0$$

from which we conclude that $M(t) = M(0) =: M_0$ for all $t \geq 0$ □

The mass conservation property for bulk–surface reaction–diffusion models has been established in different contexts (Cusseddu et al. 2018; Rätz and Röger 2012). However, to the best of our knowledge, it has never been identified in the context of oligomerization reactions.

2.4 Non-dimensionalization

We introduce a non-dimensional version of the system that allows a convenient qualitative interpretation independent of the actual system size, but instead through the ratio of kinetic parameters to the diffusion contributions. We follow the approach in Rätz and Röger (2012), Rätz (2015) and define $U, A_1, A_2, \ldots, A_N$ be the dimensional concentration quantities where $[U] = \mathrm{mol}/\mu m^3$ and $[A] = \mathrm{mol}/\mu m^2$ for $j = 1, \ldots, N$. We also define L and T as the spatial and temporal quantities, where $[L] = \mu m$ and $[T] = s$. We then introduce the non-dimensional variables

$$\hat{u} = \frac{u}{U}, \quad \hat{a}_j = \frac{a_j}{A_j} \quad (j = 1, \ldots, N), \quad \hat{t} = \frac{t}{T}, \quad \text{and} \quad \hat{x} = \frac{x}{L},$$

which lead to the transformed domains $\hat{\Omega} := \{\zeta \in \mathbb{R}^3 | \zeta L \in \Omega\}$ and $\hat{\Gamma} = \partial\hat{\Omega}$. By denoting $\hat{\nabla}$, $\hat{\nabla}^2$, and $\hat{\Delta}$ as the dimensionless gradient, Laplace, and Laplace–Beltrami operators, respectively, and using

$$\nabla = \frac{1}{L}\hat{\nabla}, \quad \nabla^2 = \frac{1}{L^2}\hat{\nabla}^2, \quad \Delta = \frac{1}{L^2}\hat{\Delta},$$

we can apply the chain rule and rewrite the system (2)–(6) in the form

$$\frac{U}{T}\frac{\partial \hat{u}}{\partial \hat{t}} = D_u \frac{U}{L^2}\hat{\nabla}^2\hat{u}, \quad \hat{x} \in \hat{\Omega}, \tag{9}$$

$$\begin{aligned}\frac{A_1}{T}\frac{\partial \hat{a}_1}{\partial \hat{t}} = {} & \frac{D_1 A_1}{L^2}\hat{\Delta}\hat{a}_1 + k_d A_1 \left\{ \left(\frac{k_0 U}{k_d A_1} + \frac{k_b A_N U}{k_d A_1}\hat{a}_N \right)\hat{u} - \hat{a}_1 \right. \\ & - 2\frac{k_m A_1}{k_d}\hat{a}_1^2 + 2\frac{k_2 A_2}{k_d A_1}\hat{a}_2 \\ & \left. - \hat{a}_1 \left(\sum_{l=2}^{N-1} \frac{A_j k_g}{k_d}\hat{a}_j \right) + \sum_{j=3}^{N} \frac{k_j A_j}{k_d A_1}\hat{a}_j \right\}, \quad \hat{x} \in \hat{\Gamma},\end{aligned} \tag{10}$$

$$\frac{A_2}{T}\frac{\partial \hat{a}_2}{\partial \hat{t}} = \frac{D_2 A_2}{L^2}\hat{\Delta}\hat{a}_2 + k_d A_1 \left(\frac{k_m A_1}{k_d}\hat{a}_1^2 - \frac{k_2 A_2}{k_d A_1}\hat{a}_2 - \frac{k_g A_2}{k_d}\hat{a}_1\hat{a}_2 + \frac{k_3 A_3}{k_d A_1}\hat{a}_3 \right), \quad \hat{x} \in \hat{\Gamma}, \tag{11}$$

$$\begin{aligned}\frac{A_j}{T}\frac{\partial \hat{a}_j}{\partial \hat{t}} = {} & \frac{D_j A_j}{L^2}\hat{\Delta}\hat{a}_j + k_d A_1 \left(\frac{k_g A_{j-1}}{k_d}\hat{a}_1\hat{a}_{j-1} - \frac{k_j A_j}{k_d A_1}\hat{a}_j - \frac{k_g A_j}{k_d}\hat{a}_1\hat{a}_j \right. \\ & \left. + \frac{k_{j+1} A_{j+1}}{k_d A_1}\hat{a}_{j+1} \right), \\ & \hat{x} \in \hat{\Gamma}, \quad j = 3, \ldots, N\end{aligned} \tag{12}$$

$$\frac{A_N}{T}\frac{\partial \hat{a}_N}{\partial \hat{t}} = \frac{D_N A_N}{L^2}\hat{\Delta}\hat{a}_N + k_d A_1 \left(\frac{k_g A_{N-1}}{k_d}\hat{a}_1\hat{a}_{N-1} - \frac{k_N A_N}{k_d A_1}\hat{a}_N \right), \quad \hat{x} \in \hat{\Gamma}. \tag{13}$$

The boundary conditions in (7) can be rewritten as

$$-\frac{D_u U}{L}\left(\mathbf{n} \cdot \nabla \hat{u}\right)\Big|_{x \in \Gamma} = k_d A_1 \left\{ \left(\frac{k_0 U}{k_d A_1} + \frac{k_b A_N}{k_d A_1}\hat{a_N} \right)\hat{u} - \hat{a_1} \right\}. \tag{14}$$

Since $R > 0$, we can define the characteristic concentrations U and A_j by dividing the total mass of the system per total volume and surface area, respectively. We also define the characteristic time with respect to the diffusion D_1 of the monomeric component across the cellular surface. Formally, we define

$$U = \frac{M_0}{R \cdot |\Gamma|}, \quad A_j = \frac{M_0}{|\Gamma|} \quad \text{for} \quad j = 1, 2, \ldots, N, \quad T = \frac{R^2}{D_1}, \quad L = R, \tag{15}$$

and the dimensionless parameters

$$\hat{k}_0 = \frac{k_0 U}{k_d A_1}, \quad \hat{k}_b = \frac{k_b A_N U}{k_d A_1}, \quad \hat{k}_m = \frac{k_m A_1}{k_d}, \quad \hat{k}_j = \frac{k_j A_j}{k_d A_1} \quad (j = 2, \ldots, N),$$
$$\hat{k}_g = \frac{k_g A_j}{k_d} \quad (j = 2, \ldots, N-1), \quad \gamma = \frac{k_d R^2}{D_1}, \quad \tilde{D} = \frac{D_u}{D_1},$$
$$d_j = \frac{D_j}{D_1} \quad (j = 2, \ldots, N).$$

As a result, (9) can be written as

$$\frac{\partial \hat{u}}{\partial \hat{t}} = \tilde{D} \hat{\nabla}^2 \hat{u}, \tag{16}$$

for $\hat{x} \in \hat{\Omega}$ with boundary condition

$$-\tilde{D} \left(\mathbf{n} \cdot \hat{\nabla} \hat{u} \right) \Big|_{x \in \Gamma} = \gamma \left\{ \left[\hat{k}_0 + \hat{k}_b \hat{a}_N \right] \hat{u} - \hat{a}_1 \right\} \tag{17}$$

for $\hat{x} \in \hat{\Gamma}$. Finally, for the surface components, (10)–(13) can be written as

$$\frac{\partial \hat{a}_1}{\partial \hat{t}} = \hat{\Delta} \hat{a}_1 + \gamma \left\{ \left[\hat{k}_0 + \hat{k}_b \hat{a}_N \right] \hat{u} - \hat{a}_1 - 2\hat{k}_m \hat{a}_1^2 + 2\hat{k}_2 \hat{a}_2 \right.$$
$$\left. -\hat{k}_g \hat{a}_1 \left(\sum_{l=2}^{N-1} \hat{a}_j \right) + \sum_{j=3}^{N} \hat{k}_j \hat{a}_j \right\}, \tag{18}$$
$$\frac{\partial \hat{a}_2}{\partial \hat{t}} = d_2 \hat{\Delta} \hat{a}_2 + \gamma \left(\hat{k}_m \hat{a}_1^2 - \hat{k}_2 \hat{a}_2 - \hat{k}_g \hat{a}_1 \hat{a}_2 + \hat{k}_2 \hat{a}_3 \right), \tag{19}$$
$$\frac{\partial \hat{a}_j}{\partial \hat{t}} = d_j \hat{\Delta} \hat{a}_j + \gamma \left(\hat{k}_g \hat{a}_1 \hat{a}_{j-1} - \hat{k}_j \hat{a}_j - \hat{k}_g \hat{a}_1 \hat{a}_j + \hat{k}_{j+1} \hat{a}_{j+1} \right), \quad j = 3, \ldots, N \tag{20}$$
$$\frac{\partial \hat{a}_N}{\partial \hat{t}} = d_N \hat{\Delta} \hat{a}_N + \gamma \left(\hat{k}_g \hat{a}_1 \hat{a}_{N-1} - \hat{k}_N \hat{a}_N \right). \tag{21}$$

2.5 System Reduction when $D_u \to \infty$

We further reduce our system by assuming the limit of rapid cytosolic diffusion, which has been experimentally observed for chemotaxis in amoebae (Postma et al. 2004), membrane-associated $PH_{\delta 1}$ molecules (Goehring et al. 2010), and several other studies [56] (Christensen et al. 2016; Adam and Delbrück 1968; Berg 1977; McCloskey and Poo 1986; Haugh and Lauffenburger 1997; Abel et al. 2012) [63]. From a modeling perspective, this assumption has also been extensively explored, especially in the context of cell polarization (Mori et al. 2008; Cusseddu et al. 2018; Rätz and Röger

2012; Trong et al. 2014). The resulting system is uniquely defined on the membrane surface, and the bulk variable u will be represented by an integral operator also called a *non-local functional*. Our approach closely follows the work of Rätz and Röger (2012), Rätz (2015), though our system can be N-dimensional in principle. Formally, if we assume $D_u \to \infty$ and if the initial concentration of $\hat{u}$ is constant over $\hat{\Omega}$, then $\hat{u}$ no longer depends on space and $u = u(t)$. Therefore, the mass conservation law given by (8) implies

$$\hat{u}(t)|\hat{\Omega}| + \sum_{j=1}^{N} \left\{ j \cdot \int_{\hat{\Gamma}} \hat{a}_j \mathrm{d}s \right\} = \mathcal{M}_0 \tag{22}$$

where $\mathcal{M}_0 = \hat{u}(0)|\hat{\Omega}| + \sum_{j=1}^{N} \left\{ j \cdot \int_{\hat{\Gamma}} \hat{a}_j(s,0)\mathrm{d}s \right\}$ is the total mass of the dimensionless system. We then define the non-local functional

$$\mathcal{U}[\hat{a}_1, \hat{a}_2, \ldots, \hat{a}_N](t) := \frac{1}{|\hat{\Omega}|} \left[\mathcal{M}_0 - \sum_{j=1}^{N} \left\{ j \cdot \int_{\hat{\Gamma}} \hat{a}_j \mathrm{d}s \right\} \right]$$

as in Rätz and Röger (2012), Rätz (2015). Finally, we drop all the hats to obtain the reduced system

$$\frac{\partial a_1}{\partial t} = \Delta a_1 + \gamma \mathcal{F}_1(a_1, a_2 \ldots, a_N) \tag{23}$$

$$\frac{\partial a_j}{\partial t} = d_j \Delta a_j + \gamma \mathcal{F}_j(a_1, a_2 \ldots, a_N), \quad j = 2, \ldots, N \tag{24}$$

where

$$\begin{aligned}
\mathcal{F}_1 &= [k_0 + k_b a_N]\mathcal{U}[a_1, a_2, \ldots, a_N] - a_1 - 2k_m a_1^2 + 2k_2 a_2 \\
&\quad - k_g a_1 \left(\sum_{l=2}^{N-1} a_j \right) + \sum_{j=3}^{N} k_j a_j, \\
\mathcal{F}_2 &= k_m a_1^2 - k_2 a_2 - k_g a_1 a_2 + k_2 a_3, \\
\mathcal{F}_j &= k_g a_1 a_{j-1} - k_j a_j - k_g a_1 a_j + k_{j+1} a_{j+1}, \quad j = 3, \ldots, N \\
\mathcal{F}_N &= k_g a_1 a_{N-1} - k_N a_N.
\end{aligned}$$

In the next sections, we will provide analytical estimates and numerical simulations to analyze the stability properties of the reduced system (23)–(24).

3 Mathematical Analysis

Obtaining the mathematical conditions for the existence of diffusion-driven instabilities is a crucial step for understanding the origin of heterogeneous steady-state

solutions (Turing 1952; Murray 1993). For membrane proteins, it has been experimentally observed that a heterogeneous distribution of protein density accounts for several processes that ensure proper cell function, such as receptor signaling, membrane polarization/depolarization, and calcium channels activity (Lao et al. 2010; Sleno and Hbert 2018; Baisamy et al. 2005). For this reason, establishing the precise role of the lateral diffusion in the generation of such heterogeneity is an important step toward a comprehensive description of pattern formation in the cellular surface.

In this section, we present the mathematical framework for investigating diffusion-driven instabilities in the system (23)–(24). We establish conditions that guarantee the existence and uniqueness of homogeneous steady states, or the conditions for having multiple steady states. We also present a characterization for the Jacobian Matrix in the case of homogeneous perturbations. For the non-homogeneous case, the linearization of the non-local functional yields a different Jacobian matrix, and a family of ordinary differential equations is derived to analyze the stability in terms of the eigenfunctions of the Laplace–Beltrami operator. We then apply our framework in the case $N = 2$, where we obtain a necessary condition for diffusion-driven instabilities. We start with the characterization of the homogeneous steady states.

3.1 Homogeneous Steady States

The homogeneous solutions of (23)–(24) satisfy the ODE system

$$\frac{da_j}{\mathrm{d}t} = \gamma \mathcal{F}_j(a_1, a_2 \ldots, a_N) \quad j = 1, \ldots, N$$

and the steady states in this case are given by $\mathbf{a}^* = (a_1^*, a_2^*, a_3^*, \ldots, a_N^*)$ such that

$$\mathcal{F}_j(\mathbf{a}^*) = 0$$

for all $j = 1, \ldots, N$. From $\mathcal{F}_N(\mathbf{a}^*) = 0$, we obtain $a_N^* = \frac{k_g a_1^* a_{N-1}^*}{k_N}$ and, proceeding recursively, it is easy to show that

$$a_j^* = \frac{k_g a_1^* a_{j-1}^*}{k_j} \quad \text{for} \quad j = 3, \ldots, N, \quad \text{and} \quad a_2^* = \frac{k_m (a_1^*)^2}{k_2}. \tag{25}$$

Hence, $a_j^* = C_j (a_1^*)^j$ where $C_1 = 1$ and

$$C_j = \left(\prod_{i=3}^{j} \frac{k_g}{k_i} \right) \left(\frac{k_m}{k_2} \right) \quad \text{for} \quad j = 2, \ldots, N.$$

Thus, from $\mathcal{F}_1(\mathbf{a}^*) = 0$, we must have

$$a_1^* = \left[k_0 + k_b\, a_N^*\right] \frac{1}{|\Omega|} \left[\mathcal{M}_0 - |\Gamma| \sum_{j=1}^{N} j \cdot a_j^*\right]$$
$$= \left[k_0 + k_b\, C_N (a_1^*)^N\right] \frac{1}{|\Omega|} \left[\mathcal{M}_0 - |\Gamma| \sum_{j=1}^{N} j \cdot C_j (a_1^*)^j\right]. \tag{26}$$

By multiplying both sides by $|\Omega|$ and rearranging the $(a_1^*)^j$ terms, we can define the polynomial

$$\mathcal{P}_N(\alpha) = -k_0\mathcal{M}_0 \; + \; (|\Omega| \; + \; k_0|\Gamma|)\,\alpha \; + \; k_0|\Gamma| \left(\sum_{j=2}^{N-1} j C_j \alpha^j\right)$$
$$+ \; C_N\,(k_0|\Gamma|N - \mathcal{M}_0 k_b)\,\alpha^N \; + \; k_b|\Gamma|C_N \left(\sum_{j=1}^{N} j C_j \alpha^{N+j}\right), \tag{27}$$

where the roots of $\mathcal{P}_N$ are the steady-state values a_1^*. We then observe that the coefficient of α^N is a nonnegative number if and only if

$$k_0|\Gamma|N - \mathcal{M}_0 k_b \geq 0,$$

which in this case implies that $\mathcal{P}_N(\alpha)$ has a unique positive root and therefore that the system has a unique steady state. This is the case when $k_b = 0$, which means that the largest oligomers do not promote ligand binding in the plasma membrane. On the other hand, if $k_0|\Gamma|N - \mathcal{M}_0 k_b < 0$, then multiple steady states could exist.

3.2 Linear Stability Analysis

Linear stability is a traditional concept from the theory of dynamical systems that treat the study of the local behavior near a steady-state solution. The term "linear" stands for the analysis of the linear approximation of a nonlinear system, which can be sufficient to determine if a steady state is stable or unstable. In the case of a system of ODEs, the analysis is carried out by evaluating the eigenvalues of the so-called Jacobian matrix. A similar analysis can be done in the context of reaction–diffusion systems of PDEs with the analysis of the eigenvectors of the Laplace operator. A major contribution in this field is due to Alan Turing in the classic paper "The Chemical Basis of Morphogenesis" (Turing 1952). Turing established the notion of diffusion-driven instabilities and was the first to connect this mathematical idea with the formation of spatially heterogeneous patterns. In what follows, we first analyze the homogeneous perturbations of the steady states by describing the Jacobian matrix of the system. Then we define the conditions for diffusion-driven instabilities in our system (23)–(24).

3.2.1 Homogeneous Perturbations

In this section, we investigate the linear stability of the steady states $\mathbf{a}^*$ against spatially homogeneous perturbations, that is, in the absence of diffusion. Our study is an N-dimensional version of the approach taken in Rätz and Röger (2012), Rätz (2015) for a GTPase cycling model. We need to compute the eigenvalues λ of the Jacobian matrix

$$\mathcal{J}[\mathbf{a}^*] = \gamma \left[\frac{\partial \mathcal{F}_j^*}{\partial a_i} \right]_{1 \le i,j \le N}$$

for $\mathcal{F}_j$ defined in (23) and (24). If all the eigenvalues of $\mathcal{J}[\mathbf{a}^*]$ have negative real parts, then the steady state is called linearly stable (Strogatz 1994). That means that local perturbations will converge to the steady state.

On the other hand, if at least one of the eigenvalues has a positive real part, then it is called linearly unstable, in which local perturbations will lead the system away from the steady state. The next proposition generally characterizes $\mathcal{J}[\mathbf{a}^*] - \lambda \mathbf{I}$.

Proposition 3.1 *The matrix $\mathcal{J}[\boldsymbol{a}^*] - \lambda \boldsymbol{I}$ can be written in the form*

$$\begin{bmatrix} w_0 - \lambda & \boldsymbol{w} \\ \boldsymbol{v} & H - \lambda \boldsymbol{I} \end{bmatrix}$$

where w_0 and λ are real numbers, $\boldsymbol{w} \in \mathbb{R}^{N-1}$ is a row vector, $\boldsymbol{v} \in \mathbb{R}^{N-1}$ is a column vector, and H is a $(N-1) \times (N-1)$ tridiagonal matrix.

Proof We will first calculate $\frac{\partial \mathcal{F}_j^*}{\partial a_i}$ for $i, j = 1, 2, \ldots, N$. For $j = 1$, we obtain

$$\begin{aligned}
\frac{\partial \mathcal{F}_1^*}{\partial a_1} &= -\frac{|\Gamma| \left(k_0 + k_b a_N^*\right)}{|\Omega|} - 1 - 4k_m a_1^* - \sum_{l=2}^{N-1} k_g a_l^*, \\
\frac{\partial \mathcal{F}_1^*}{\partial a_2} &= -2\frac{|\Gamma| \left(k_0 + k_b a_N^*\right)}{|\Omega|} - k_g a_1^* + 2k_2, \\
\frac{\partial \mathcal{F}_1^*}{\partial a_i} &= -i\frac{|\Gamma| \left(k_0 + k_b a_N^*\right)}{|\Omega|} - k_g a_1^* + k_i \quad \text{for} \quad i = 3, 4, \ldots, N-1, \\
\frac{\partial \mathcal{F}_1^*}{\partial a_N} &= -N\frac{|\Gamma| \left(k_0 + k_b a_N^*\right)}{|\Omega|} + \frac{k_b}{|\Omega|} \left(\mathcal{M}_0 - |\Gamma| \sum_{j=1}^{N} j \cdot a_j^* \right) + k_N.
\end{aligned}$$

Now for $j = 2$, we have

$$\frac{\partial \mathcal{F}_2^*}{\partial a_1} = 2k_m a_1^* - k_g a_2^*, \quad \frac{\partial \mathcal{F}_2^*}{\partial a_2} = -k_g a_1^* - k_2, \quad \frac{\partial \mathcal{F}_2^*}{\partial a_3} = k_3 \quad \frac{\partial \mathcal{F}_2^*}{\partial a_i} = 0, \quad i = 4, 5, \ldots, N$$

and for $j = 3$ to $j = N - 1$, we obtain

$$\frac{\partial \mathcal{F}_j^*}{\partial a_1} = k_g a_{j-1}^* - k_g a_j^*, \quad \frac{\partial \mathcal{F}_j^*}{\partial a_{j-1}} = k_g a_1^*, \quad \frac{\partial \mathcal{F}_j^*}{\partial a_j} = -k_g a_1^* - k_j, \quad \frac{\partial \mathcal{F}_j^*}{\partial a_{j+1}} = k_{j+1},$$

and

$$\frac{\partial \mathcal{F}_j^*}{\partial a_i} = 0,$$

otherwise, and finally for $j = N$,

$$\frac{\partial \mathcal{F}_N^*}{\partial a_1} = k_g a_{N-1}^*, \quad \frac{\partial \mathcal{F}_N^*}{\partial a_2} = k_g a_1^*, \quad \frac{\partial \mathcal{F}_N^*}{\partial a_N} = -k_N, \quad \text{and} \quad \frac{\partial \mathcal{F}_N^*}{\partial a_i} = 0 \quad \text{otherwise.}$$

We then define $\mathcal{J}_{ij}^* := \gamma \frac{\partial \mathcal{F}_j^*}{\partial a_i}$, $w_0 := \mathcal{J}_{11}^* - \lambda$, the vectors $\mathbf{v}, \mathbf{w} \in \mathbb{R}^{N-1}$ such that

$$\mathbf{v} = \left(\mathcal{J}_{21}^* \ \mathcal{J}_{31}^* \cdots \mathcal{J}_{N1}^*\right)^T \quad \text{and} \quad \mathbf{w} = \left(\mathcal{J}_{12}^* \ \mathcal{J}_{13}^* \cdots \mathcal{J}_{1N}^*\right)$$

and

$$H = \begin{bmatrix} \mathcal{J}_{22}^* - \lambda & \mathcal{J}_{23}^* & 0 & \cdots & 0 & 0 & 0 \\ \mathcal{J}_{32}^* & \mathcal{J}_{33}^* - \lambda & \mathcal{J}_{34}^* & \cdots & 0 & 0 & 0 \\ \vdots & \vdots & \vdots & \vdots & \vdots & \vdots & \vdots \\ 0 & 0 & 0 & \cdots & \mathcal{J}_{N-1N-2}^* & \mathcal{J}_{N-1N-1}^* - \lambda & \mathcal{J}_{N-1N}^* \\ 0 & 0 & 0 & \cdots & 0 & \mathcal{J}_{NN-1}^* & \mathcal{J}_{NN}^* - \lambda \end{bmatrix}_{(N-1)\times(N-1)}$$

which proves the proposition. □

3.2.2 Non-homogeneous Perturbations

We now consider a perturbation of the form $\mathbf{a}_s = (a_{s,1}, a_{s,2}, \ldots, a_{s,N})$ for $s \in (-1, 1)$ of the homogeneous steady state $\mathbf{a}^*$ in the direction of $\Phi = (\varphi_1, \varphi_2, \ldots, \varphi_N)$, for non-homogeneous $\varphi_j : \Gamma \times (0, T) \to \mathbb{R}$. Thus, for each component, we assume

$$a_{s,j}|_{s=0} = a_j^* \quad \text{and} \quad \left.\frac{\partial a_{s,j}}{\partial s}\right|_{s=0} = \varphi_j,$$

so we may write the linear approximation $a_{s,j} \approx a_j^* + s\varphi_j$ for $j = 1, \ldots, N$

$$a_{s,j} = a_j^* + s\ \varphi_j(x, t).$$

In particular, the linearization of the non-local functional yields $\mathcal{U}[\mathbf{a}_s] \approx \mathcal{U}[\mathbf{a}^*] + s(\frac{\mathrm{d}}{\mathrm{d}s}\big|_{s=0}\mathcal{U}[\mathbf{a}_s])$ where

$$\left(\frac{\mathrm{d}}{\mathrm{d}s}\bigg|_{s=0}\mathcal{U}[\mathbf{a}_s]\right) = -\sum_{j=1}^{N}\frac{\mathrm{d}}{\mathrm{d}s}\bigg|_{s=0}\int_\Gamma a_{s,j}\mathrm{d}s = -\sum_{j=1}^{N}\int_\Gamma \varphi_j \mathrm{d}s. \tag{28}$$

Since we assume that $\varphi_j \in L^2(\Gamma)$ are orthogonal to the constant perturbations, which were analyzed in the previous section, we now consider

$$\int_\Gamma \varphi_j \mathrm{d}s = 0 \quad \text{for} \quad j = 1, \ldots, N,$$

which leads to a linearized system with a constant input $\mathcal{U}[\mathbf{a}_s](t) = \mathcal{U}[\mathbf{a}^*]$. For the approximation of the component a_1, we thus have

$$\partial_t \varphi_1 = \Delta\varphi_1 + \sum_{j=1}^{N}\tilde{\mathcal{J}}_{1,j}(\mathbf{a}^*)\varphi_j, \tag{29}$$

where

$$\tilde{\mathcal{J}}_{1,1} = -\gamma\left\{1 + 4k_m a_1^* + k_g\left(\sum_{l=2}^{N-1} a_l^*\right)\right\}, \quad \tilde{\mathcal{J}}_{1,2}(\mathbf{a}^*) = \gamma\left(2k_2 - k_g a_1^*\right),$$
$$\tilde{\mathcal{J}}_{1,j}(\mathbf{a}^*) = \gamma\left(k_j - k_g a_j^*\right), \quad j = 3, \ldots, N-1, \quad \text{and} \quad \tilde{\mathcal{J}}_{1,N}(\mathbf{a}^*) = \gamma\left(k_N + k_b\,\mathcal{U}[\mathbf{a}^*]\right).$$

The other terms of the Jacobian matrix remain the same as in the case of the homogeneous perturbations, so we omit the explicit calculations. In vector notation, we can then write the linearized system in the form

$$\partial_t \Phi = \mathbf{D}\Delta\Phi + \tilde{\mathcal{J}}(\mathbf{a}^*)\Phi, \tag{30}$$

where $\mathbf{D}$ is a diagonal matrix such that $\mathbf{D}_{jj} = d_j$ where $d_1 = 1$ and $\tilde{\mathcal{J}}(\mathbf{a}^*)$ is the modified Jacobian matrix. We then define $\mathbb{N}_0 := \mathbb{N} \cup \{0\}$ and consider $(\omega_l)_{l\in\mathbb{N}_0} \subset L^2(\Gamma)$, an orthonormal basis of infinitely smooth eigenfunctions of the Laplace–Beltrami operator, i.e.,

$$-\Delta\omega_l = \eta_l\omega_l. \quad \text{where} \quad 0 = \eta_0 < \eta_1 \leq \eta_2 \leq \cdots.$$

In the case where Γ is the unitary sphere $\mathbb{S}^2$ parametrized by the angles $\phi \in [0, 2\pi)$ and $\theta \in [0, \pi)$, the eigenfunctions have the closed form

$$\cos(m\phi)P_k^m(\cos(\theta)) \quad \text{and} \quad \sin(m\phi)P_k^m(\cos(\theta))$$

where $k \geq 0$, $0 \leq m \leq k$ and $P_k^m(t)$ are the so-called *associated Legendre function* (see references Gallier 2009; Silverman 1972 for details).

Then, for each $j = 1, \ldots, N$ we can express each component φ_j as a linear combination

$$\varphi_j = \alpha_{j0}\, \omega_0 + \sum_{l \in \mathbb{N}} \alpha_{jl}\, \omega_l$$

where $\alpha_{jl} = \alpha_{jl}(t)$ for $l \in \mathbb{N}_0$. Using vector notation, we can define the quantity $\mathcal{A}_l = (\alpha_{1l}, \alpha_{2l}, \ldots, \alpha_{Nl})^T$ such that

$$\Phi = \mathcal{A}_0\, \omega_0 + \sum_{l \in \mathbb{N}} \mathcal{A}_l\, \omega_l(x).$$

By substituting the above expansion in (30), we obtain the linear ODE system

$$\frac{\mathrm{d}\mathcal{A}_l}{\mathrm{d}t} = \left[-\eta_l \mathbf{D} + \gamma \tilde{\mathcal{J}}(\mathbf{a}^*)\right] \mathcal{A}_l \quad \text{for} \quad l = 0, 1, 2, \ldots \tag{31}$$

and diffusion-driven instabilities occur if the above system is unstable for some $l \in \mathbb{N}_0$. This is true when at least one eigenvalue λ of the matrix $-\eta_l \mathbf{D} + \tilde{\mathcal{J}}(\mathbf{a}^*)$ has a positive real part. Therefore, our target quantity is the so-called *dispersion relation*

$$h(l) := \max\left(\mathrm{Re}(\lambda(\eta_l))\right), \tag{32}$$

where $\mathrm{Re}(z)$ denotes the real part of a complex number z. Finally, the characteristic polynomials $p_l(\lambda) := \det(\lambda \mathbf{I} - \gamma \tilde{\mathcal{J}}(\mathbf{a}^*) + \eta_l \mathbf{D})$ can be written in the form

$$p_l(\lambda) = \lambda^N + b_{l,N-1}\lambda^{N-1} + \ldots + b_{l,0}$$

where $b_{l,0} = \det(-\gamma \tilde{\mathcal{J}}(\mathbf{a}^*) + \eta_l \mathbf{D})$. Therefore, if $b_{l,0} < 0$ for some $l \in \mathbb{N}$, and since $p_l(\tilde{\lambda}) > 0$ for $\tilde{\lambda}$ sufficiently large ($p_l(\lambda) \to \infty$ as $\lambda \to \infty$), the intermediate value theorem ensures that p_l has a positive root in $[0, \tilde{\lambda}]$ and therefore $h(l) > 0$.

3.3 Special Case $N = 2$: Necessary Conditions for Diffusion-Driven Instabilities

We now fix $N = 2$ and analyze the conditions for diffusion-driven instabilities. The equations are given by

$$\partial_t a_1 = \Delta a_1 + \gamma \left\{ \frac{(k_0 + k_b a_2)}{|\Omega|} \left[\mathcal{M}_0 - \int_\Gamma (a_1 + 2a_2)\, \mathrm{d}s \right] - a_1 - 2k_m a_1^2 + 2k_2 a_2 \right\} \tag{33}$$

$$\partial_t a_2 = d_2 \Delta a_2 + \gamma \left\{ k_m a_1^2 - k_2 a_2 \right\} \tag{34}$$

and describe the simplest case where a reversible *dimerization* (formation of oligomers of size two) occurs on the plasma membrane. Dimerization in the cellular surface is a

key factor in regulation and takes place for numerous molecules, such as ion channels (Marianayagam et al. 2004), receptor tyrosine kinases (RTKs) Lemmon and Schlessinger (2010); Sarabipour and Hristova (2016), and K-ras GTPases (Muratcioglu et al. 2015). From a mathematical perspective, the case $N = 2$ is more tractable and therefore can potentially give some insight into the mechanisms of pattern formation in our model. On the other hand, even this simple case differs substantially from the previous work of Rätz and Röger (2012, 2014), Rätz (2015), since we only assume reversible mass action instead of Michaelis–Menten kinetics, and also because of the particular positive feedback (Eq. 1) that has not been considered in previous studies.

We provide a necessary condition in a particular case where the system admits a unique spatially homogeneous steady state. We prove that the system does not exhibit diffusion-driven instabilities provided that k_b is sufficiently small. In biological terms, the following result states that if the A_N-dependent binding rate of monomers to the membrane is low enough, which can be interpreted as a small influence of the largest oligomers in the binding process, then diffusive effects will dominate, and no protein distribution heterogeneity will form on the cellular surface.

Theorem 3.1 *Suppose $k_b \geq 0$ is such that*

$$k_b \leq \frac{2}{\mathcal{M}_0} \min\left\{k_0|\Gamma|, \frac{d_2\eta_i|\Omega|}{\gamma}\right\}$$

for all $i \in \mathbb{N}$. Then, the system admits a unique steady state and no diffusion-driven instability exists.

Proof Let $\mathbf{a}^* = \left(a_1^*, a_2^*\right)$ be the spatially homogeneous steady $\mathbf{a}^* = \left(a_1^*, a_2^*\right)$, which is obtained when $a_2^* = \frac{k_m (a_1^*)^2}{k_2}$ and a_1^* is a solution of $\mathcal{P}_2(\alpha) = 0$, where

$$\begin{aligned}\mathcal{P}_2(\alpha) = &-k_0\mathcal{M}_0 + (|\Omega| + k_0|\Gamma|)\,\alpha + \frac{k_m}{k_2}\left(2k_0|\Gamma| - \mathcal{M}_0 k_b\right)\alpha^2 \\ &+ k_b|\Gamma|\frac{k_m}{k_2}\alpha^3 + 2\left(\frac{k_m}{k_2}\right)^2 k_b|\Gamma|\alpha^4.\end{aligned}$$

Now since $k_b \leq \frac{2k_0|\Gamma|}{\mathcal{M}_0}$, we have $2k_0|\Gamma| - \mathcal{M}_0 k_b \geq 0$, and therefore, $\mathcal{P}_2$ has only nonnegative coefficients except $-k_0\mathcal{M}_0$, which implies that $\mathcal{P}_2(\alpha)$ strictly increases for $\alpha \geq 0$. On the other hand, $\mathcal{P}_2(\alpha) \to \infty$, and hence, $\mathcal{P}_2(\tilde{\alpha}) > 0$ for $\tilde{\alpha}$ sufficiently large. The intermediate value theorem then ensures that the system admits a unique positive steady state in $[0, \tilde{\alpha}]$. The Jacobian matrix with respect to homogeneous perturbations is then given by

$$\mathcal{J}[\mathbf{a}^*] = \gamma \begin{bmatrix} -1 - 4a_1^* k_m - \frac{|\Gamma|}{|\Omega|}\left(\frac{k_b k_m (a_1^*)^2}{k_2} + k_0\right) & 2a_1^* k_m \\ 2k_2 + \frac{k_b}{|\Omega|}\left[\mathcal{M}_0 - \left(\frac{2k_m (a_1^*)^2}{k_2} + a_1^*\right)|\Gamma|\right] - \frac{2|\Gamma|}{|\Omega|}\left(\frac{k_b k_m (a_1^*)^2}{k_2} + k_0\right) & -k_2 \end{bmatrix}$$

with a second-order characteristic polynomial $p(\lambda) = \det(\lambda \mathbf{I} - \mathcal{J}[\mathbf{a}^*])$ given by $p(\lambda) = \lambda^2 + b\lambda + c$, where

$$b = \gamma \left(\frac{(a_1^*)^2 |\Gamma| k_b k_m}{k_2 |\Omega|} + 4 a_1^* k_m + \frac{|\Gamma| k_0}{|\Omega|} + k_2 + 1 \right) > 0$$

and

$$c = \gamma^2 \left(\frac{8(a_1^*)^3 |\Gamma| k_b k_m^2}{k_2 |\Omega|} + \frac{3(a_1^*)^2 |\Gamma| k_b k_m}{|\Omega|} + \frac{2 a_1^* k_m}{|\Omega|} (2|\Gamma| k_0 - k_b \mathcal{M}_0) + \frac{|\Gamma| k_0 k_2}{|\Omega|} + k_2 \right)$$

is also positive because $2k_0|\Gamma| - \mathcal{M}_0 k_b \geq 0$. From that, we conclude that both eigenvalues

$$\lambda = \frac{-b \pm \sqrt{b^2 - 4c}}{2}$$

must have real negative parts, and therefore, the steady states are linearly stable. We then perform a similar argument for non-homogeneous perturbations. From (29), we obtain the modified Jacobian matrix $\tilde{\mathcal{J}}(\mathbf{a}^*)$, and for a given $l \in \mathbb{N}_0$, we have

$$\tilde{\mathcal{J}}(\mathbf{a}^*) - \eta_l \mathbf{D} = \begin{bmatrix} -\gamma(1 + 4 a_1^* k_m) - \eta_l & \gamma \left\{ 2k_2 + \frac{k_b}{|\Omega|} \left[\mathcal{M}_0 - |\Gamma| \left(\frac{2k_m (a_1^*)^2}{k_2} + a_1^* \right) \right] \right\} \\ 2\gamma \, a_1^* \, k_m & -\gamma \, k_2 - d_2 \eta_l \end{bmatrix}$$

with characteristic polynomials $p_l(\lambda) := \det(\lambda \mathbf{I} - \gamma \tilde{\mathcal{J}}(\mathbf{a}^*) + \eta_l \mathbf{D})$ given by the quadratics $p_l(\lambda) = \lambda^2 + b_l \lambda + c_l$, where

$$b_l = \gamma \, (4 a_1^* k_m + k_2 + 1) + \eta_l (d_2 + 1) > 0$$

and

$$c_l = \left[d_2 \eta_l^2 + \gamma \eta_l (d_2 + k_2) + \gamma^2 k_2 \right] + 2 \, \gamma k_m \, a_1^* \left(2 d_2 \eta_l - \frac{\gamma k_b \mathcal{M}_0}{|\Omega|} \right) + \frac{2\gamma^2 (a_1^*)^2 |\Gamma| k_b k_m}{|\Omega|} \left(1 + \frac{2 a_1^* k_m}{k_2} \right).$$

In the case $l \in \mathbb{N}$, the c_l terms are also positive, since we assume

$$k_b \leq \frac{2 d_2 \eta_l |\Omega|}{\gamma \mathcal{M}_0} \iff 2 d_2 \eta_l - \frac{\gamma k_b \mathcal{M}_0}{|\Omega|} \geq 0 \quad \forall i \in \mathbb{N},$$

and in this case the $p_l(\lambda)$ have no roots with positive real parts. In the case $l = 0$, we know that $\eta_0 = 0$, but the modified matrix $\tilde{\mathcal{J}}(\mathbf{a}^*)$ yields a different linearized system.

Thus, we have to analyze the stability of the linear equation given in (31) in the case where $l = 0$, i.e.,

$$\frac{d\mathcal{A}_0}{dt} = \left[\gamma \tilde{\mathcal{J}}(\mathbf{a}^*)\right]\mathcal{A}_0$$

with characteristic polynomial $p_0(\lambda) = \lambda^2 + b_0\lambda + c_0$ where

$$b_0 = \gamma\ (4a_1^* k_m + k_2 + 1) > 0$$

and

$$\begin{aligned} c_0 &= \gamma^2 \left\{ k_2 - 2k_m\ a_1^* \left(\frac{k_b \mathcal{M}_0}{|\Omega|}\right) + \frac{2(a_1^*)^2 |\Gamma| k_b k_m}{|\Omega|}\left(1 + \frac{2a_1^* k_m}{k_2}\right)\right\} \\ &= \gamma^2 \left\{ k_2 - \frac{2k_m k_b a_1^*}{|\Omega|}\left[\mathcal{M}_0 - |\Gamma|\left(a_1^* + 2\frac{(a_1^*)^2 k_m}{k_2}\right)\right]\right\}. \end{aligned} \tag{35}$$

We now verify that $c_0 \geq 0$. In fact, from (26) when $N = 2$, we obtain

$$\frac{1}{|\Omega|}\left[\mathcal{M}_0 - |\Gamma|\left(a_1^* + 2\frac{(a_1^*)^2 k_m}{k_2}\right)\right] = \frac{k_2 a_1^*}{\left[k_0 k_2 + k_b (a_1^*)^2 k_m\right]},$$

and therefore by substituting the above equation on (35) and using that $a_2^* = \frac{k_m}{k_2}(a_1^*)^2$, we obtain

$$c_0 = \gamma^2 k_2 \left\{ 1 - 2\ \frac{a_2^*}{\left[\frac{k_0}{k_b} + a_2^*\right]} \right\}.$$

Finally, the hypothesis gives us $\frac{k_0}{k_b} \geq \frac{\mathcal{M}_0}{2|\Gamma|}$ and by using $\mathcal{M}_0 - 2|\Gamma| a_2^* \geq 0$ (total mass of a_2 at steady state does not exceeds the total mass of the system) we obtain $\frac{\mathcal{M}_0}{2|\Gamma|} \geq a_2^*$ and therefore

$$\frac{a_2^*}{\left[\frac{k_0}{k_b} + a_2^*\right]} \leq \frac{1}{2}$$

from which we conclude that $c_0 \geq 0$. Therefore, the steady state is stable against non-constant perturbations. □

4 Numerical Simulations

We perform numerical simulations to complete our mathematical analysis. In sect. 3, we established the mathematical framework for investigating the existence

of diffusion-driven instabilities and obtained a necessary condition in the case $N = 2$. However, no sufficient conditions were explored, and no further analysis was done for $N > 2$. For this reason, we complete our analysis by searching for linear instabilities in the parameter space and analyzing the single-patch steady state that forms when the parameters lie in the instability regions. In terms of biological motivation, our analytical estimates provided no conditions that guarantee the formation of spatial patterns, which in turn are known to exist in the plasma membrane in various contexts. Therefore, we can use numerical simulations to obtain heterogeneous patterns and analyze their spatial properties.

We start the section by analyzing the parameter regions of bistability (Sect. 4.1). Then, we investigate whether the stable steady states become linearly unstable under non-homogeneous perturbations (Sect. 4.2). From the linear instability analysis, we obtain the *single-patch* non-homogeneous steady state (Sect. 4.3). Finally, we study the temporal dynamics of pattern formation (Sect. 4.4) and the single-patch dependence on the cell radius (Sect. 4.5). The numerical simulations were implemented in MATLAB R2018a and Comsol Multiphysics 5.4. In subsections 7.1.1 and 7.1.2 in the Electronic Supplementary Material (ESM), we provide the numerical details of our simulations.

4.1 Bistability Under Homogeneous Perturbations

We begin by computing the homogeneous steady states $\mathbf{a}^*$ and the corresponding eigenvalues of the Jacobian matrix $\mathcal{J}[\mathbf{a}^*]$ under homogeneous perturbations (cf. Sect. 3.2.1). We then explore the parameter regions of bistability where the system admits three steady states, two of them stable and one unstable. In the case $N = 2$, we obtain regions of bistability by change the basal binding rate k_0 and the A_2-dependent binding rate k_b (Fig. 2). For $k_0 = 0.015$, three steady-state values for a_1^* emerge depending on k_b (Fig. 2a). When k_0 also changes, we obtain both a *bistability region* (dark gray) and a *single steady-state region* (light gray) (Fig. 2b). A colored (red, black, and blue) vertical line represents the region from Fig. 2a. Other parameter choices also lead to bistability regions (see Figure S1 (A) for $N = 2$ and Figure S2 (A) for $N = 3$ in the (ESM)).

4.2 Linear Instability Under Non-homogeneous Perturbations

In this section, we numerically investigate which parameter values promote linear instability under non-homogeneous perturbations. We fix an eigenmode index $l \geq 1$ to explore diffusion-driven instabilities, and let $\mathbf{a}^*$ be a stable steady state under homogeneous perturbations. We can thus compute the dispersion relation $h(l)$ [Eq. (32)] defined in Sect. 3.2.2 by calculating the roots of the characteristic polynomials $p_l(\lambda)$. This step was done using the function *eig* in MATLAB R2018a (see subsection 7.1.1 in the ESM for further details on our MATLAB simulations). If $h(l) < 0$, the steady state remains stable in the direction of the chosen eigenmode. In this case, the analysis is inconclusive, since we would also need to determine the stability for the other eigenmodes. If $h(l) > 0$, the steady state becomes unstable for the chosen eigenmode, and this is sufficient to ensure a diffusion-driven instability (Smith and

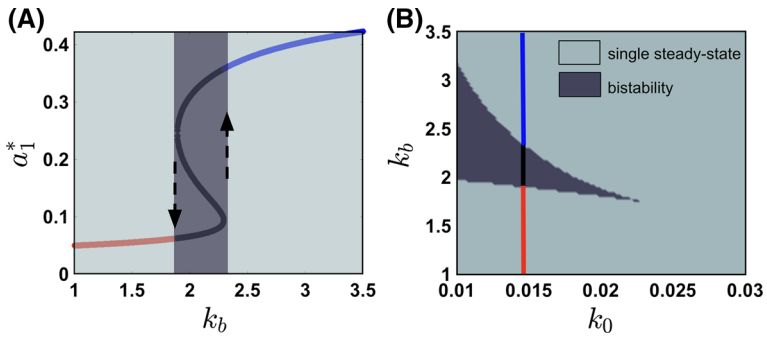

Fig. 2 Steady states and parameter regions for bistability ($N = 2$). **a** The value of $k_0 = 0.015$ is fixed, while k_b ranges from 1 to 3.5. We then compute the steady states, which are the solution of (26). The single steady-state branches are shown in red and blue, respectively, while the bistable branch is shown in black. The dark gray rectangle illustrates the emergence of bistability, and the dashed black arrows indicate the stable steady states. **b** Bistability region for $k_0 \in [0.01, 0.03]$ with $k_0 = 0.015$ marked. The dark gray region contains the k_b values for which the system admits a bistability region. The single steady-state regions are indicated in light gray. The remaining fixed parameters: $R = 1$, $\Gamma = 4\pi$, $\Omega = \frac{3}{4}\pi$, $\mathcal{M}_0 = \Gamma$, $k_m = 1$, and $k_2 = 1$ (Color figure online)

Dalchau 2018). The case $h(l) = 0$ usually requires higher-order analysis, so we will not consider it in the context of linear stability.

Given a fixed eigenmode index l, we can then divide the parameter space into four regions. We will call them Regions 0, 1, 2, and 3, where the numbers reflect the exact number of unstable steady states (Fig. 3a) for $N = 2$ and (b) for $N = 3$. More precisely, we define:

- *Region 0* The single steady-state region where $h(l) < 0$, there are no unstable steady states.
- *Region 1* The single steady-state region where $h(l) > 0$, there is only *one* unstable steady state.
- *Region 2* The bistability region where $h(l) > 0$ for only one stable steady state, a total of *two* unstable steady states.
- *Region 3* The bistability region where $h(l) > 0$ for both stable steady states, a total of *three* unstable steady states.

The stability analysis in Region 0 is more subtle and requires further analysis since the stability criterion needs to be fulfilled for all eigenmodes. However, at least for $N = 2$, Theorem 3.1 ensures that the system remains stable for sufficiently small k_b, which appears to be consistent with the numerical predictions. For higher k_b values, the instabilities emerge in the bistability region (Regions 2 and 3) and also in the single steady-state Regions 0 and 1. We obtain a similar result for $N = 3$ (Fig. 3b). However, it should be noticed that the k_b values promoting linear instabilities are higher (see y-axis ranging from 4 to 14) compared with the case $N = 2$. Regions 0, 1, 2, and 3 can be found with other parameter choices (see Figure S1 (B) for $N = 2$ and Figure S2 (B) for $N = 3$ in the ESM).

Region 1 is known as a *Turing-type instability region* (Turing 1952; Murray 1993), where the system may converge to a spatially non-homogeneous steady state. We

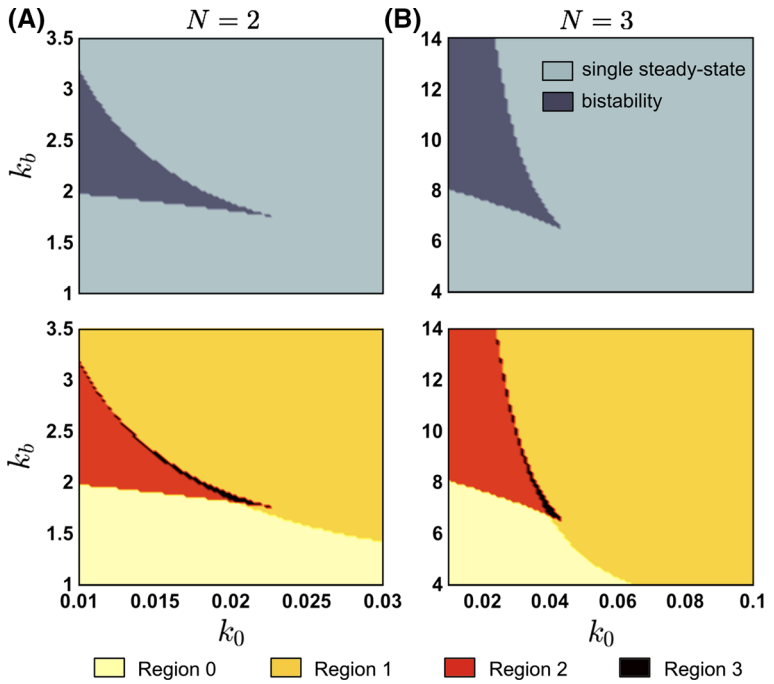

Fig. 3 Parameter regions of bistability and linear instability ($N = 2$ and $N = 3$). We scan the reaction rates for different parameter values. In the top, the parameter regions in the $k_0 \times k_b$ plane where the system exhibits bistability under homogeneous perturbations. In the bottom, Regions 0, 1, 2, and 3 divide the $k_0 \times k_b$ plane according to the number of unstable steady states under non-homogeneous perturbations for the eigenmode $l = 1$ (see text for details). **a** $N = 2$, $d_2 = 0.1$, $\gamma = 1000$. **b** $N = 3$, $d_2 = d_3 = 0.1$, $\gamma = 1000$. The k_b values that promote linear instability are significantly higher for $N = 3$ compared to the case $N = 2$. Remaining fixed parameters: $R = 1$, $\Gamma = 4\pi$, $\Omega = \frac{3}{4}\pi$, $\mathcal{M}_0 = \Gamma$, $k_2 = k_3 = 1$, and $k_m = k_g = 1$ (Color figure online)

analyze this region when we increase both k_0 and k_b ranges for different values of the diffusion coefficient d_2 (Fig. 4a). As d_2 decreases, Region 1 increases, which illustrates how the system becomes unstable as the discrepancies between diffusion become higher. A similar phenomenon occurs as we increase the dimensionless parameter γ, also referred to as the *Damköhler number* (Scott 2005), which is the rate of membrane dissociation of monomers compared to their diffusivity. Increasing γ allows a higher dominance of the reaction flux over diffusion effects (Burke and Schumann 1928), and thus, a larger unstable space tends to occur (Figure S3). On the other hand, as the eigenmode index l increases, Region 1 significantly decreases (Fig. 4b). We exhibit the results for $l = 2$, $l = 6$, and $l = 8$. Such a decrease implies that the Region 1 for the higher eigenmodes ($l > 1$) is contained in the Region 1 for the first eigenmode ($l = 1$). For this reason, to determine the whole instability region in this case (which is the union of Regions 1 for all eigenmodes), it is sufficient to consider Region 1 for $l = 1$.

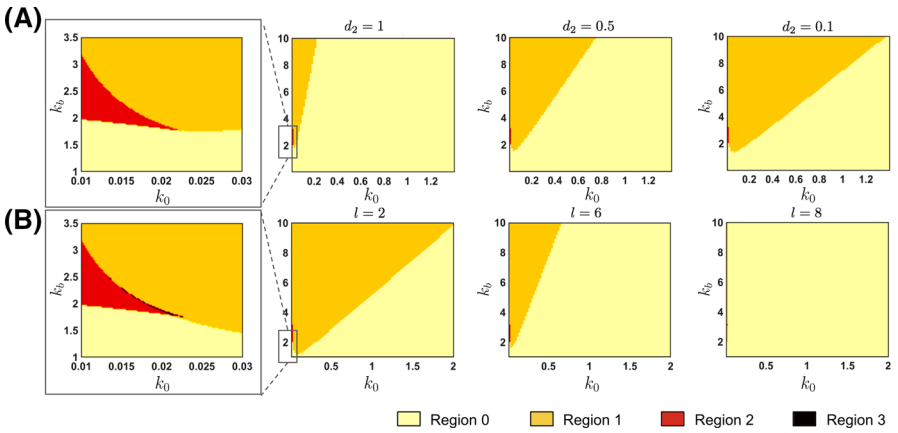

Fig. 4 Changing the diffusion coefficient and the eigenmode of the Laplace–Beltrami operator for $N = 2$. **a** For $d_2 = 1$, we show a zoomed plot of the interface of the Regions 1 and 2. Most of the (k_0, k_b) in the rectangle $[0.01, 1.4] \times [1, 10]$ belongs to the Region 0, where the system is stable under non-homogeneous perturbations. However, by decreasing d_2 to 0.5 and further to 0.1, the Region 1 (in orange) significantly increases, which means that the system exhibits a larger instability region for lower d_2 values. In this figure, we fix $\gamma = 10$ and $l = 1$ as the eigenmode index. **b** Linear instability Region 1 for eigenmode index values $l = 2$, 6, and 8. For $l = 2$, the system is unstable under non-homogeneous perturbations for most (k_0, k_b) values above the diagonal of the rectangle $[0.01, 2] \times [1, 10]$. As l increases, Region 1 (in orange) significantly decreases. Therefore, we can analyze the instability of the system by exploring only the first eigenmode, since Region 1 does not expand as l increases. In this figure, we fix $\gamma = 100$ and $d_2 = 0.1$. Remaining fixed parameters: $R = 1$, $\Gamma = 4\pi$, $\Omega = \frac{3}{4}\pi$, $\mathcal{M}_0 = \Gamma$, $k_2 = 1$, and $k_m = 1$ (Color figure online)

4.3 The Emergence of the Single-Patch Non-homogeneous Steady State

In this section, we investigate the spatiotemporal behavior of our system by numerically integrating the dimensionless equations. We consider a spherical domain of radius $R = 1$ and, as in the previous sections, we fix $N = 2$ or $N = 3$. We avoid solving the surface system (23)–(24) due to the numerical complexity of the non-local functional. Instead, we solve the dimensionless bulk–surface Eqs. (16)–(21) (dropping all the hats) for an extremely high cytosolic diffusion ($\tilde{D} = 10^8$) on (16). In this way, our resulting system can be seen as an approximation of the reduced system when $\tilde{D} \to \infty$. We randomly perturbed the homogeneous steady states by considering a small number $\varepsilon > 0$ as the perturbation magnitude and a family $\{\xi(x)\}_{x\in\Gamma}$ of independent random variables uniformly distributed between -1 and 1. In the case where $N = 2$, we define the surface initial conditions

$$a_1(x, 0) := a_1^* + \varepsilon\, \xi(x) \quad \text{and} \quad a_2(x, 0) := a_2^* - \frac{1}{2}\varepsilon\, \xi(x) \tag{36}$$

for $x \in \Gamma$, where the $\frac{1}{2}$ accounts for mass conservation [see (22)]. For the volume component, we define $u(x, 0) := u^*$, for $x \in \Omega$, where $u^* = \frac{1}{|\Omega|}\left[\mathcal{M}_0 - |\Gamma|(a_1^* + 2a_2^*)\right]$ also because of the mass conservation property. For $N = 3$, we define a_1^*

as in (36), $a_j(x,0) := a_j^* - \frac{1}{5}\varepsilon\ \xi(x)$ for $j = 2$ and $j = 3$, and $u^* = \frac{1}{|\Omega|}\left[\mathcal{M}_0 - |\Gamma|(a_1^* + 2a_2^* + 3a_3^*)\right]$.

Remark 4.1 The element $(a_1^*, a_2^*, \ldots, a_N^*)$ is a homogeneous steady state of the system (23)–(24) if and only if $(a_1^*, a_2^*, \ldots, a_N^*, u^*)$ is a homogeneous steady state of the system (16)–(21) provided that

$$u^* = \frac{1}{|\Omega|}\left[\mathcal{M}_0 - |\Gamma|(a_1^* + 2a_2^* + \ldots + Na_N^*)\right].$$

From the remark above, we can obtain the steady states of the reduced system (23)–(24). Then, we can numerically integrate the bulk–surface PDE system (16)–(21) using the perturbation scheme described above. In order to associate the parameter regions that lead to instabilities with the formation of spatial patterns, we select four (k_0, k_b) values in the four Regions 0, 1, 2, and 3 (Fig. 5). We fix $N = 2$ and the eigenmode index $l = 1$. For each choice of (k_0, k_b) , we integrate the system (16)–(21) to its final state by perturbing a homogeneous steady state. We then plot the result for the a_1 component and visually inspect the results. For (k_0, k_b) in Regions 1, 2, and 3, (colored in orange, red, or black, respectively), a *single-patch* spatially heterogeneous steady state emerges. On the other hand, when (k_0, k_b) belong to Region 0, in which the system is stable for the eigenmode index $l = 1$, the system converges to its homogeneous steady state. This result indicates that the single-patch pattern is consistent across parameter choices in Regions 1, 2, and 3, once it remains unchanged in its circular shape and gradient of concentrations. Figure S4 in the ESM shows a similar result in the case $N = 3$.

4.4 Temporal Evolution and Pattern Formation

In this section, we further investigate the temporal evolution of the system. We consider $N = 2$ and $(k_0, k_b) = (0.025, 2.5)$ which belongs to Region 1 (see Fig. 5). We then observe the spatial distribution of a_1 for different times (Fig. 6a). At $t = 0$, We apply a random perturbation of magnitude $\varepsilon = 10^{-10}$ around the unique homogeneous steady state that is unstable under non-homogeneous perturbations. The system then smooths due to diffusion, and the small random peaks continuously coalesce and react, until a few large domains emerge at $t = 0.099$. At $t = 0.114$ and $t = 0.119$, multiple patches of higher a_1 concentration emerge. The feedback term [Eq. (1)] then plays its role, once the higher a_2 concentration location promotes the recruitment of more cytosolic component. This leads to the formation of the single-patch profile at $t = 0.159$. From that time until the final time ($t = 1$), the spatial configuration only changes in terms of concentration gradients. File F1 in the ESM contains a movie of the simulation shown in Fig. 6a for both monomeric (a_1) and dimeric components (a_2). In Figure S5 in the ESM, we show a similar result for $N = 3$.

In order to quantify the single-patch size, we quantify the surface area of the high-concentration locations in the spherical domain. For this purpose, we define the function

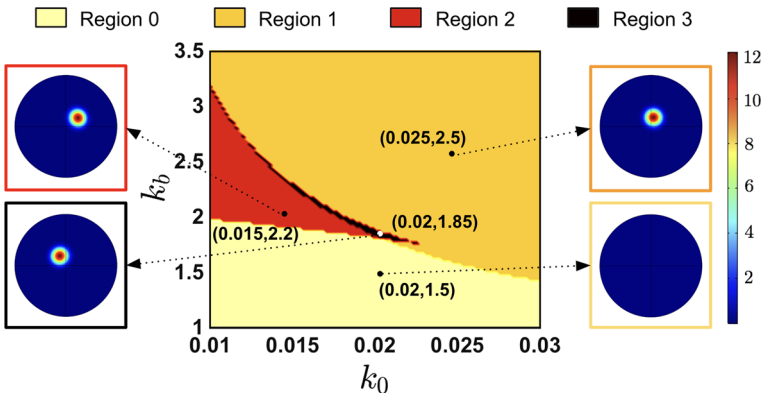

Fig. 5 Linear instability and pattern formation ($N = 2$). We exhibit the stability analysis colormap for eigenmode index $l = 1$ and the final spatial profile of the a_1 component. We consider four (k_0, k_b) values from Regions 0, 1, 2, and 3, which are colored in light yellow, orange, red, or black, respectively. For Regions 1, 2, and 3, we observe the emergence of a single-patch spatially heterogeneous steady state which is consistent across parameter regions in terms of its circular shape and concentration gradient. For Region 0, we do not observe a pattern formation for this particular eigenmode. In this figure, $d_2 = 0.1$, $\gamma = 1000$, $k_m = k_2 = 1$; steady-state values: Region 0: $a_1^* = 0.0812$, $a_2^* = 0.0066$, $u^* = 2.7168$. Region 1: $a_1^* = 0.3817$, $a_2^* = 0.1457$, $u^* = 0.9806$. Region 2: $a_1^* = 0.2759$, $a_2^* = 0.0761$, $u^* = 1.7155$. Region 3: $a_1^* = 0.1107$, $a_2^* = 0.0123$, $u^* = 2.5942$. Remaining fixed parameters: $R = 1$, $\Gamma = 4\pi$, $\Omega = \frac{3}{4}\pi$, $\mathcal{M}_0 = \Gamma$, $k_2 = 1$, $k_m = 1$ (Color figure online)

$$\mathcal{I}_{a_j}^{\varepsilon}(t) = \int_{\Gamma} \mathbb{1}_{\{a_j(x,t) > \langle a_j \rangle(t) + \varepsilon\}} \mathrm{d}s \tag{37}$$

where ε is the perturbation magnitude, j is the index of the oligomeric component, and $\langle a_j \rangle(t) = \int_{\Gamma} a_j \mathrm{d}s$ is the average concentration of a_j across the sphere Γ. We then evaluate the evolution of $\mathcal{I}_{a_j}^{\varepsilon}(t)$ over time (Fig. 6b). We exhibit the results of a single simulation for $N = 2$ and $N = 3$, and $\varepsilon = 10^{-10}$. At early times, when the concentrations a_j are close to the steady state a_j^* across the domain, $\mathcal{I}_{a_j}^{\varepsilon}(t)$ remains close to 0. Then, the combination of diffusion and the feedback term makes the concentration gradients increase in a large portion of the domain, as illustrated in Fig. 6a for $t = 0.099$, $t = 0.114$, and $t = 0.119$. Finally, the formation of the single patch promotes the decrease of $\mathcal{I}_{a_j}^{\varepsilon}(t)$, since the area of high concentration tends to be small in comparison with the total surface area. Moreover, the concentration outside the patch tends to be small, which makes the average $\langle a_j \rangle(t)$ assume lower values. Therefore, in the final times, the locations in the sphere where the concentrations remain above the average can be associated with the single patch. For this reason, we define the *single-patch area*

$$\mathcal{S}_{a_j}^{\varepsilon} := \mathcal{I}_{a_j}^{\varepsilon}(t_f),$$

where t_f is the final simulation time. In this work, we avoid an analytical treatment for the functions $\mathcal{I}_{a_j}^{\varepsilon}(t)$. In particular, we base our definition of the single-patch area $\mathcal{S}_{a_j}^{\varepsilon}$ on visual inspection of the curves in Fig. 6b: for $N = 2$ and $N = 3$, the quantities

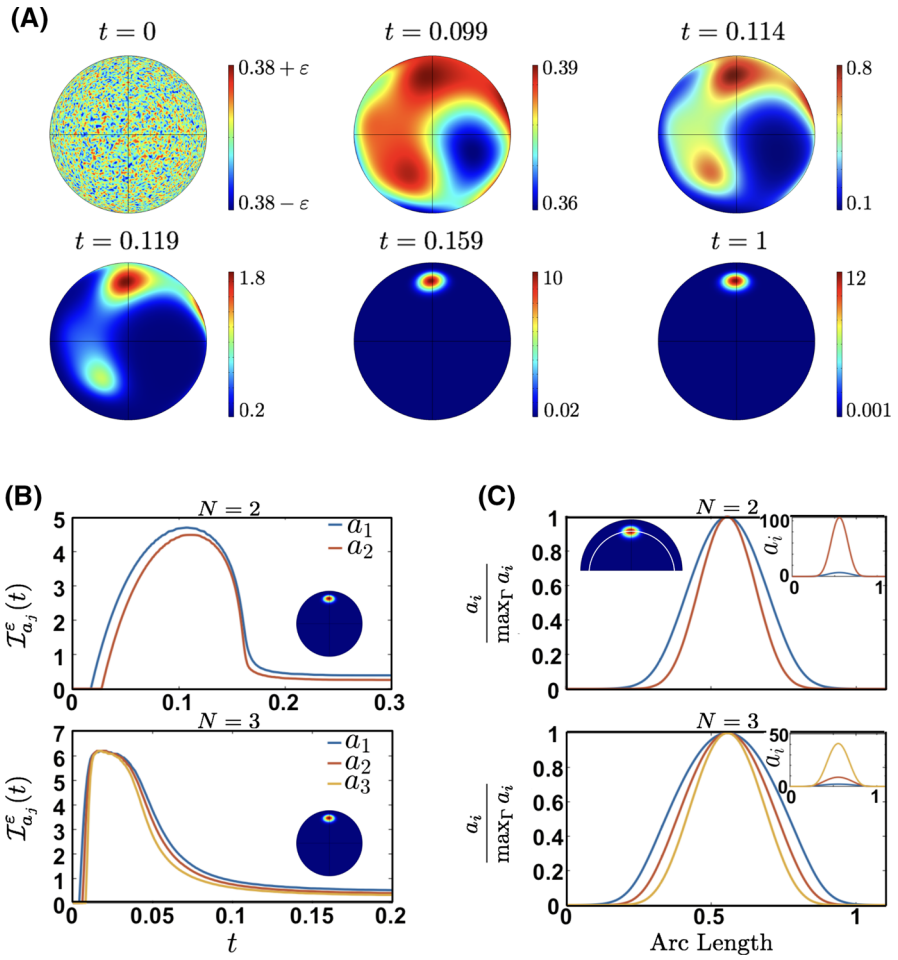

Fig. 6 Temporal evolution and pattern formation **a** Spatial distribution of the monomeric component (a_1) at different non-dimensional times. At $t = 0$, a random perturbation of magnitude $\varepsilon = 10^{-10}$ is applied to the unstable homogeneous steady state. At $t = 0.099$, a small gradient emerges until $t = 0.114$, and at $t = 0.119$, the high-concentration domains begin to coalesce. At $t = 0.159$, the system converges to the single-patch profile. Finally, at $t = 1$, we show the single-patch steady state with a final concentration gradient from 0.001 to 12 a.u. In this figure, we consider $N = 2$, $k_0 = 0.025$, and $k_b = 2.5$ such that a single steady state becomes unstable under non-homogeneous perturbations [(k_0, k_b) belongs to Region 1 in Figure 5]. The steady state is given by $a_1^* = 0.3817$, $a_2^* = 0.1457$, and $u^* = 0.9806$. A supplemental movie for panel (A) can be found in supplemental file F1. Remaining fixed parameters: $R = 1$, $\Gamma = 4\pi$, $\Omega = \frac{3}{4}\pi$, $\mathcal{M}_0 = \Gamma$, $k_2 = 1$, $k_m = 1$. **b** Evolution of $(\mathcal{I}^{\varepsilon}_{a_j})(t)$ that gives the single-patch area $\mathcal{S}^{\varepsilon}_{a_j}$ for $N = 2$ and $N = 3$ (see text for details). Inset: a single-patch final configuration. Parameter values: $R = 1$, $\gamma = 1000$, $d_2 = d_3 = 0.1$, $k_0 = 0.016$, $k_m = 1$, and $k_2 = 0.44$. Top: $N = 2$, $k_b = 1$. Bottom: $N = 3$, $k_b = 10$, $k_g = k_m$, $k_3 = k_2$. Initial conditions: $a_1(0) = 0.0918$, $a_2(0) = 0.0191$, $a_3(0) = 0$, $u(0) = 2.6099$. **c** For $N = 2$ and $N = 3$, we plot the final normalized a_j concentrations on a geodesic curve parametrized by arc-length. As the oligomer index j increases, the distribution and maximum value of a_j becomes tighter and higher (inset), respectively (Color figure online)

$\mathcal{I}^{\varepsilon}_{a_1}(t)$ converge to a final value after a transient increase and subsequent decrease in time. Thus, we assume that this final value gives a good estimate of the single-patch area as a function ε. In Figure S6 in the ESM, we illustrate how the percentage of $\mathcal{S}^{\varepsilon}_{a_j}$ with respect to the total surface area does not change significantly as ε changes. We also observe that $\mathcal{I}^{\varepsilon}_{a_1} > \mathcal{I}^{\varepsilon}_{a_2}$ for all times in the case where $N = 2$, and also $\mathcal{I}^{\varepsilon}_{a_1} > \mathcal{I}^{\varepsilon}_{a_2} > \mathcal{I}^{\varepsilon}_{a_3}$ in the case where $N = 3$. We conclude that $\mathcal{S}^{\varepsilon}_{a_1} > \mathcal{S}^{\varepsilon}_{a_2}$ (for $N = 2$) and $\mathcal{S}^{\varepsilon}_{a_1} > \mathcal{S}^{\varepsilon}_{a_2} > \mathcal{S}^{\varepsilon}_{a_3}$ (for $N = 3$). In order to better visualize this area shrinking as the oligomer size increases, we plot the final normalized concentration profiles (Fig. 6c). Given the arc-length parametrization of a geodesic curve crossing the single-patch region, the concentration distributions become tighter for a_2 compared to a_1 in the case $N = 2$. The inset plot shows the non-normalized concentrations, where we see that $a_2 > a_1$ in the single-patch location. A similar phenomenon occurs for $N = 3$: the distribution and maximum value of a_j becomes tighter and larger as j increases from 1 to 3.

4.5 Change of the Cell Radius and Single-Patch Area

We investigate how the single-patch area of a spherical cell depends on its radius R. From the non-dimensionalization of the bulk–surface system (see Sect. 2.4), we defined the characteristic quantities (15). In order to move through a dimensional system, we define the dimensionless parameters as depending on R to preserve a constant volume concentration. Therefore, we assume a constant U such that $\mathcal{M}_0 \propto R^3$, making the dimensionless parameters functions of R. For this reason, each choice of R will lead to a different solution of the non-dimensional system (16)–(21). In particular, it will also change the non-dimensional single-patch area $\mathcal{S}^{\varepsilon}_{a_j}$. We show the results for R ranging from 0.5 to 5 and two different parameters (Fig. 7):

$$\text{area percentage} = \frac{\mathcal{S}^{\varepsilon}_{a_j}}{4\pi} \times 100 \quad \text{and} \quad \text{dimensional area} = \mathcal{S}^{\varepsilon}_{a_j}\, R^2.$$

For $N = 2$ and $N = 3$, we provide the same total volume concentration for the system. For clarity, in this section we will refer to the non-dimensional system with the hat ($\hat{}$) notation. We define the initial conditions as a linear ramp of slope ε around the steady state

$$\hat{a}_1(x, 0) = \hat{a}_1^* + \varepsilon\, \hat{x}_1 \quad \text{and} \quad \hat{a}_2(x, 0) = \hat{a}_2^* - \frac{1}{2}\, \varepsilon\, \hat{x}_1,$$

where $\hat{x} = (\hat{x}_1, \hat{x}_2, \hat{x}_3) \in \hat{\Gamma}$ and $\hat{x}_1$ is the position with the sphere centered in the origin. In the case $N = 3$, we assumed $a_3^* = 0$. See Fig. 7 caption for details on the parameter choices. We then observe the same phenomena: the dimensional area (Fig. 7 red; open circles) increases approximately linearly with R. On the other hand, the area percentage (Fig. 7 black; closed circles) decreases with R. We can then conclude that although the dimensional area of clusters increases, the additional spherical area changes at a much faster rate since the area percentage varies with $\approx \frac{1}{R}$. The effect of

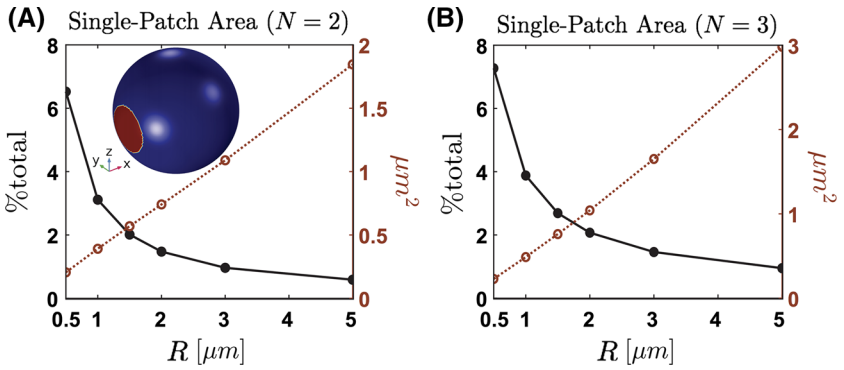

Fig. 7 Change of the cell radius and single-patch area. We quantify the percentage of the total area and the dimensional area (see text for details), for various radii R ranging from 0.5 to 5. The R value was changed in the non-dimensional system with a fixed concentration (U) through variations in Γ, γ, A, $\hat{k}_0$, $\hat{k}_m$, and $\hat{k}_g$ (see Eqs. 16–21). **a** We quantify the Patch size for the $N = 2$ case (red; open circles) and then normalized against the total area of the sphere (black; closed circles). As the radius increases, the patch size increases approximately linearly, but the percent area decreases rapidly. **b** The same simulation for $N = 3$. As the radius increases, the patch size increases, but the total percent area still decreases. Between cases, we observe the same general qualitative properties for single-patch area percentage and dimensional area. The major differences arise in the absolute values, as $N = 3$ creates larger patches. In these simulations, $\varepsilon = 0.01a_2^*$, $a_1^* = 0.0981$, $a_2^* = 0.0191$, $a_3^* = 0$, $u^* = 2.6099$. Parameter values: $d_2 = d_3 = 0.1$, $\tilde{D} = 10^8$, $\hat{k}_0 = \frac{0.016}{R}$, $\hat{k}_b = 10$, $\hat{k}_g = \hat{k}_m = R$, $\hat{k}_3 = \hat{k}_2 = 0.44$, $\gamma = 1000R^2$ (Color figure online)

N on single-patch area shows both dimensional area and area percentage are higher for $N = 3$ (Fig. 7b) in comparison with $N = 2$ (Fig. 7a).

5 Discussion

Protein heterogeneity in the PM is of critical importance to cellular functions. Many factors influence this heterogeneity, including membrane composition, protein–protein interaction, phase separation, lateral diffusion, and possible feedback, resulting in the formation of spatial patterns (Hashimoto and Panchenko 2010; Johannes et al. 2018; Ispolatov 2005). For this reason, understanding the interplay of aggregation kinetics, lateral diffusion, and feedback in the formation of spatial patterns is an essential step toward developing a complete description of the mechanisms behind protein clustering on the cell surface. In this work, we developed a bulk–surface model for protein aggregation with positive feedback that exhibits a spatially heterogeneous single-patch steady state. To the best of our knowledge, this is the first modeling attempt that merges the reaction–diffusion version of classical Smoluchowski dynamics with the modern bulk–surface geometrical setup.

A major result from our model is the role played by the feedback term $k_b\, a_N$ in the boundary conditions (1). If k_b is low enough, the steady-state distribution is spatially uniform, and no protein heterogeneity exists. For $N = 2$, we formally proved such a result (Theorem 3.1), and for $N = 3$, we used numerical simulations to observe a similar phenomenon. In particular, in the total absence of feedback ($k_b = 0$),

we observed that spatial heterogeneity is not achievable when we only considered protein–protein interaction. On the other hand, if k_b is sufficiently high, we observed the emergence of linear instability and therefore patterning on the cellular surface. Experimental observations have shown that membrane proteins do organize in a spatially heterogeneous fashion (Choquet 2010; Gan et al. 2015; Padmanabhan et al. 2019). However, the molecular mechanisms are still being investigated experimentally. The feedback mechanism we proposed here can also be interpreted in purely biological terms. The largest oligomers recruit ligands from the cytosol, which form ligand–receptor monomers. If the rate of recruitment of monomers is low, diffusive effects dominate, and the configuration of the system is homogeneous in space. On the other hand, a higher rate promotes a significant influx of new monomeric components. Then, continued oligomerization generates higher concentrations of the largest components, which closes the positive feedback loop and drives pattern formation. The largest oligomers can thus be interpreted as self-activators of pattern formation. For this reason, our mechanism of pattern formation can be related to the classical Turing framework, where self-activation is required to generate spatial patterns (Turing 1952; Gierer and Meinhardt 1972). Another interesting aspect of our model is the absence of an explicit description of cooperative binding. For the wave-pinning model (Mori et al. 2008, 2011; Cusseddu et al. 2018), cooperativity is included with a Hill function, which accounts for the positive feedback. In contrast, our oligomerization reactions assume only mass action kinetics, which seems to be insufficient for pattern formation without the feedback term.

Bistable systems are well known to promote diffusion-driven instabilities in the context of cell polarization (Rappel and Edelstein-Keshet 2017; Semplice et al. 2012). For the wave-pinning model (Mori et al. 2008, 2011; Cusseddu et al. 2018), the structure of the Hill function is responsible for bistability. Other studies followed a similar approach, using a particular choice of reaction flux that is naturally associated with a bistable regime (Beta et al. 2008; Alonso and Baer 2010). In our model, bistability emerges by the combination of two key ingredients: positive feedback and mass conservation. This observation becomes clear as we carefully inspect the steady-state analysis of the reduced system (cf. Sect. 3.1). First, the equilibrium of the oligomerization reactions (driven only by mass action kinetics) provides the distribution across different surface components. Then, the input from the non-local functional comes into play, as a consequence of the boundary conditions and mass conservation. The non-local functional at steady state provides an extra equation, which gives the equilibrium solutions for the monomeric component. The particular contribution of the feedback comes from the coefficient $C_N\,(k_0|\Gamma|N - \mathcal{M}_0 k_b)\,\alpha^N$ of the polynomial $\mathcal{P}_N(\alpha)$. If the coefficient is negative, then the existence of three roots, and therefore three steady states, is achievable. In this case, we can compute their stability under homogeneous perturbations and verify bistability.

Under non-homogeneous perturbations, one or two stable steady states may become unstable, and the system undergoes a diffusion-driven instability. Even more impressive is the emergence of a linear instability parameter region, called Region 1 in this study, when the system admits a single steady state that becomes unstable. We note that in Getz et al. (2018), the authors were able to find a region of linear instability for the wave-pinning model that is comparable with our Region 1. While the authors

briefly discussed the changes in that parameter region for different wave numbers, here we explicitly showed that the leading eigenmode exhibits a region of instability that shrinks as the eigenmode index increases. Such instability in the lower modes, which are associated with the smallest positive eigenvalues of the Laplace–Beltrami operator, has been often related to a single-patch steady-state pattern (Rätz and Röger 2014; Goryachev and Pokhilko 2008), which is confirmed for our system.

The single-patch steady state consistently appears for parameter values corresponding to different instability regions (called as Regions 0, 1,2 and 3). Goryachev and Pokhilko (2008) found a similar spatial profile for the Cdc42 GTPase cycle, where the influx of new cytoplasmic components maintained the cluster steady state and compensated for its lateral diffusion. A similar phenomenon seems to happen in our system. An allegory that explains the stable existence of such heterogeneous steady states is the so-called rich gets richer competition (Manor and Shnerb 2006). In this case, larger domains outcompete the smaller until only one stable domain arises. Our hypothesis about the existence of the single patch is based on the role of the positive feedback term. We assume that the presence of high concentrations of the largest oligomer promotes ligand binding onto the PM in a linear fashion, without any saturation mechanism or steric effects. As in Goryachev and Pokhilko (2008), this assumption seems to account for a resource competition that excludes the possibility of multiple patches. In cells, multiple patches of protein aggregates are observed (Han et al. 2017). The number and size of these aggregates often depend on the particular experimental condition and the membrane composition. Modeling such observations will require the development of a more thermodynamically detailed model.

Based on the insights from our model, we identify future research directions that will enhance studies such as ours. In the current formulation, we lack a formal explanation for the emergence and robustness of the single-patch steady state. The spatial aspects of the model render such analysis hard, but it may be possible to obtain a formal proof by considering a one-dimensional version of our system as in Mori et al. (2008). Another interesting quantity to be computed in future studies is the so-called *amplitude of the pattern*, for which a formal calculation was recently developed (Chen and Buceta 2019). Additionally, the mathematical challenge for a theoretical stability result lies in the increasing complexity of the system as N increases. In this case, we have relied on numerical simulations for $N = 3$ to identify the threshold phenomenon for diffusion-driven instabilities. However, future efforts in this direction could open up new mathematical avenues for stability analysis of increasingly complex systems. Regarding the parameter choices, its important to acknowledge that our parameters were not informed by data. Instead, in this work we focused on establishing the dimensionless parameter spaces that yield linear instabilities within the Turing approach. In a different direction, future efforts will be devoted to adapting our system to specific biological problems. Finally, including the role of curvature and cytosolic diffusion in the formation of membrane protein aggregates would bring us closer to analyses of biological and biophysical systems. These are topics of ongoing studies in our group.

Acknowledgements This work was supported by Air Force Office of Scientific Research (AFOSR) Multidisciplinary University Research Initiative (MURI) Grant FA9550-18-1-0051 to P. Rangamani. M. Holst

was supported in part by NSF Awards DMS 1620366 and DMS 1345013. We also thank the Ph.D students Jennifer Fromm, Allen Leung, and Kiersten Scott from the Rangamani Lab for the comments and feedback.

References

Abel SM, Roose JP, Groves JT, Weiss A, Chakraborty AK (2012) The membrane environment can promote or suppress bistability in cell signaling networks. J Phys Chem B 116(11):3630–3640

Achdou Y, Franchi B, Marcello N, Tesi MC (2013) A qualitative model for aggregation and diffusion of β-amyloid in Alzheimer's disease. J Math Biol 67(6–7):1369–1392

Adam G, Delbrück M (1968) Reduction of dimensionality in biological diffusion processes. Struct Chem Mol Biol 198:198–215

Albersheim P, Anderson-Prouty AJ (1975) Carbohydrates, proteins, cell surfaces, and the biochemistry of pathogenesis. Annu Rev Plant Physiol 26(1):31–52

Alonso S, Baer M (2010) Phase separation and bistability in a three-dimensional model for protein domain formation at biomembranes. Phys Biol 7(4):046012

Amestoy P, Buttari A, Duff I, Guermouche A, LExcellent JY, Uçar B (2011) Mumps. Encyclopedia of parallel computing, pp 1232–1238

Andreasen M, Lorenzen N, Otzen D (2015) Interactions between misfolded protein oligomers and membranes: a central topic in neurodegenerative diseases? Biochim et Biophys Acta-Biomembr 1848(9):1897–1907

Anoop R, Ralf L (2018) Membranes as modulators of amyloid protein misfolding and target of toxicity. Biochim Biophys Acta Biomembr 1860(9):1863–1875

Arosio P, Rima S, Lattuada M, Morbidelli M (2012) Population balance modeling of antibodies aggregation kinetics. J Phys Chem B 116(24):7066–7075

Arosio P, Knowles TPJ, Linse S (2015) On the lag phase in amyloid fibril formation. Phys Chem Chem Phys 17(12):7606–7618

Baisamy L, Jurisch N, Diviani D (2005) Leucine zipper-mediated homo-oligomerization regulates the Rho–GEF Activity of AKAP-Lbc. J Biol Chem 280(15):15405–15412

Bentz J, Nir S (1981) Mass action kinetics and equilibria of reversible aggregation. J Chem Soc Faraday Trans 1 Phys Chem Condens Ph 77(6):1249–1275

Berg HC (1977) E.M. Purcell physics of chemoreception. Biophys J 20:193–219

Bertsch M, Franchi B, Marcello N, Tesi MC, Tosin A (2016) Alzheimer's disease: a mathematical model for onset and progression. Math Med Biol J IMA 34(2):193–214

Beta C, Amselem G, Bodenschatz E (2008) A bistable mechanism for directional sensing. N J Phys 10(8):083015

Burke SP, Schumann TEW (1928) Diffusion flames. Ind Eng Chem 20(10):998–1004

Changeux J-P, Thiéry J, Tung Y, Kittel C (1967) On the cooperativity of biological membranes. Proc Natl Acad Sci U S A 57(2):335

Chatani E, Yamamoto N (2018) Recent progress on understanding the mechanisms of amyloid nucleation. Biophys Rev 10(2):527–534

Chen CP, Posy S, Ben-Shaul A, Shapiro L, Honig BH (2005) Specificity of cell–cell adhesion by classical cadherins: critical role for low-affinity dimerization through-strand swapping. Proc Natl Acad Sci 102(24):8531–8536

Choquet D (2010) Fast AMPAR trafficking for a high-frequency synaptic transmission. Eur J Neurosci 32(2):250–260

Christensen SM, Tu H-L, Jun JE, Alvarez S, Triplet MG, Iwig JS, Yadav KK, Bar-Sagi D, Roose JP, Groves JT (2016) One-way membrane trafficking of sos in receptor-triggered ras activation. Nat Struct Mol Biol 23(9):838

Cohen SIA, Vendruscolo M, Dobson CM, Knowles TPJ (2012) From macroscopic measurements to microscopic mechanisms of protein aggregation. J Mol Biol 421(2–3):160–171

Darnell JE, Lodish HF, Baltimore D et al (1990) Molecular cell biology, vol 2. Scientific American Books, New York

Davide C, Leah E-K, Mackenzie John A, Stéphanie P, Anotida M (2018) A coupled bulk–surface model for cell polarisation. J Theor Biol 481:119–135

Denk J, Kretschmer S, Halatek J, Hartl C, Schwille P, Frey E (2018) MinE conformational switching confers robustness on self-organized Min protein patterns. Proc Natl Acad Sci 115(18):4553–4558
Diegmiller R, Montanelli H, Muratov CB, Shvartsman SY (2018) Spherical caps in cell polarization. Biophys J 115(1):26–30
Drake RL (1972) A general mathematical survey of the coagulation equation. Top Curr Aerosol Res (Part 2) 3(Part 2):201–376
Erwin F, Jacob H, Simon K, Petra S (2018) Protein pattern formation. Physics of biological membranes. Springer, Berlin, pp 229–260
Franchi B, Lorenzani S (2016) From a microscopic to a macroscopic model for Alzheimer disease: two-scale homogenization of the Smoluchowski equation in perforated domains. J Nonlinear Sci 26(3):717–753
Gallier Jean (2009) Notes on spherical harmonics and linear representations of lie groups. preprint
Gan Q, Salussolia CL, Wollmuth LP (2015) Assembly of AMPA receptors: mechanisms and regulation. The Journal of Physiology 593(Pt 1):39–48
Getz MC, Nirody JA, Rangamani P (2018) Stability analysis in spatial modeling of cell signaling. Wiley Interdiscip Rev Syst Biol Med 10(1):e1395
Gierer A, Meinhardt H (1972) A theory of biological pattern formation. Kybernetik 12(1):30–39
Giese W, Eigel M, Westerheide S, Engwer C, Klipp E (2015) Influence of cell shape, inhomogeneities and diffusion barriers in cell polarization models. Phys Biol 12(6):066014
Goehring NW, Chowdhury D, Hyman AA, Grill SW (2010) FRAP analysis of membrane-associated proteins: lateral diffusion and membrane-cytoplasmic exchange. Biophys J 99(8):2443–2452
Goryachev AB, Pokhilko AV (2008) Dynamics of Cdc42 network embodies a Turing-type mechanism of yeast cell polarity. FEBS Lett 582(10):1437–1443
Guidotti G (1972) The composition of biological membranes. Arch Intern Med 129(2):194–201
Habchi J, Chia S, Galvagnion C, Michaels TCT, Bellaiche MMJ, Ruggeri FS, Sanguanini M, Idini I, Kumita JR, Sparr E, Linse S, Dobson CM, Knowles TPJ, Vendruscolo M (2018) Cholesterol catalyses β42 aggregation through a heterogeneous nucleation pathway in the presence of lipid membranes. Nat Chem 10(6):673–683
Han S, Kollmer M, Markx D, Claus S, Walther P, Fändrich M (2017) Amyloid plaque structure and cell surface interactions of β-amyloid fibrils revealed by electron tomography. Sci Rep 7:43577
Hashimoto K, Panchenko AR (2010) Mechanisms of protein oligomerization, the critical role of insertions and deletions in maintaining different oligomeric states. Proc Natl Acad Sci 107(47):20352–20357
Haugh JM, Lauffenburger DA (1997) Physical modulation of intracellular signaling processes by locational regulation. Biophys J 72(5):2014–2031
Holmes BB, Diamond MI (2012) Cellular mechanisms of protein aggregate propagation. Curr Opin Neurol 25(6):721–726
Ispolatov I (2005) Binding properties and evolution of homodimers in protein-protein interaction networks. Nucleic Acids Res 33(11):3629–3635
Jain MK, Wagner RC (1988) Introduction to biological membranes. Wiley, New York
Jarrett JT, Lansbury PT Jr (1993) Seeding one-dimensional crystallization of amyloid: a pathogenic mechanism in alzheimer's disease and scrapie? Cell 73(6):1055–1058
Johannes L, Pezeshkian W, Ipsen JH, Shillcock JC (2018) Clustering on Membranes: fluctuations and More. Trends Cell Biol 28(5):405–415
Johnson SM, Connelly S, Fearns C, Powers ET, Kelly JW (2012) The transthyretin amyloidoses: from delineating the molecular mechanism of aggregation linked to pathology to a regulatory-agency-approved drug. J Mol Biol 421(2–3):185–203
Kholodenko Boris N (2006) Cell-signalling dynamics in time and space. Nat Rev Mol cell Biol 7(3):165–176
Khuc TP, Nicola Ernesto M, Goehring Nathan W, Vijay KK, Grill Stephan W (2014) Parameter-space topology of models for cell polarity. J Phys 16(6):065009
Lao QZ, Kobrinsky E, Liu Z, Soldatov NM (2010) Oligomerization of $Ca_v\beta$ subunits is an essential correlate of Ca2+ channel activity. J Fed Am Soc Exp Biol 24(12):5013–5023
Lemmon Mark A, Joseph S (2010) Cell signaling by receptor tyrosine kinases. Cell 141(7):211–225
Lorent JH, Diaz-Rohrer B, Lin X, Spring K, Gorfe AA, Levental KR, Levental I (2017) Structural determinants and functional consequences of protein affinity for membrane rafts. Nat Commun 8(1):1219
Madzvamuse A, Chung AHW, Venkataraman C (2015) Stability analysis and simulations of coupled bulk–surface reaction–diffusion systems. Proc R Soc A Math Phys Eng Sci 471(2175):20140546–20140546
Manor A, Shnerb NM (2006) Dynamical failure of Turing patterns. Europhys Lett 74(5):837

Marianayagam NJ, Sunde M, Matthews JM (2004) The power of two: protein dimerization in biology. Trends Biochem Sci 29(11):618–625
McCloskey MA, Poo MM (1986) Rates of membrane-associated reactions: reduction of dimensionality revisited. J Cell Biol 102(1):88–96
Meisl G, Kirkegaard JB, Arosio P, Michaels TCT, Vendruscolo M, Dobson CM, Linse S, Knowles TPJ (2016) Molecular mechanisms of protein aggregation from global fitting of kinetic models. Nat Protoc 11(2):252
Mori Y, Jilkine A, Edelstein-Keshet L (2008) Wave-pinning and cell polarity from a bistable reaction–diffusion system. Biophys J 94(9):3684–3697
Mori Y, Jilkine A, Edelstein-Keshet L (2011) Asymptotic and bifurcation analysis of wave-pinning in a reaction–diffusion model for cell polarization. SIAM J Appl Math 71(4):1401–1427
Muratcioglu S, Chavan TS, Freed BC, Jang H, Lyuba Khavrutskii R, Freed N, Dyba MA, Stefanisko K, Tarasov SG, Gursoy A et al (2015) GTP-dependent K-Ras dimerization. Structure 23(7):1325–1335
Murray JD (1993) Mathematical biology, 2nd edn. Springer, New York
Padmanabhan P, Martinez-Mairmol R, Xia D, Gotz J, Meunier FA (2019) Frontotemporal dementia mutant Tau promotes aberrant Fyn nanoclustering in hippocampal dendritic spines. eLife 8:e45040
Porat-Shliom N, Milberg O, Masedunskas A, Weigert R (2013) Multiple roles for the actin cytoskeleton during regulated exocytosis. Cell Mol Life Sci 70(12):2099–2121
Postma M, Bosgraaf L, Loovers HM, Van Haastert PJM (2004) Chemotaxis: signalling modules join hands at front and tail. EMBO Rep 5(1):35–40
Rangamani P, Lipshtat A, Azeloglu EU, Calizo RC, Hu M, Ghassemi S, Hone J, Scarlata S, Neves SR, Iyengar R (2013) Decoding information in cell shape. Cell 154(6):1356–1369
Rappel W-J, Edelstein-Keshet L (2017) Mechanisms of cell polarization. Curr Opin Syst Biol 3:43–53
Rätz A (2015) Turing-type instabilities in bulk–surface reaction–diffusion systems. J Comput Appl Math 289:142–152
Rätz A, Röger M (2012) Turing instabilities in a mathematical model for signaling networks. J Math Biol 65(6–7):1215–1244
Rätz A, Röger M (2014) Symmetry breaking in a bulk-surface reaction–diffusion model for signalling networks. Nonlinearity 27(8):1805
Rosa C, Rocha Fernando A, Damas Ana M, Martins Pedro M (2012) A generic crystallization-like model that describes the kinetics of amyloid fibril formation. J Biol Chem 287(36):30585–30594
Sarabipour S, Hristova K (2016) Mechanism of FGF receptor dimerization and activation. Nat Commun 7:10262
Sarkar B, Das A, Maiti S (2013) Thermodynamically stable amyloid-β monomers have much lower membrane affinity than the small oligomers. Front Physiol 4:84
Scott FH (2005) Elements of chemical reaction engineering, 4th edn. Prentice Hall, New Jersey
Semplice M, Veglio A, Naldi G, Serini G, Gamba A (2012) A bistable model of cell polarity. PLoS ONE 7(2):e30977
Sholpan A, Xiaoguang Y, Lee James C-M (2011) Impacts of membrane biophysics in Alzheimer's disease: from amyloid precursor protein processing to β peptide-induced membrane changes. Int J Alzheimer's Dis 17(2011):134971
Silverman RA et al (1972) Special functions and their applications. Courier Corporation, North Chelmsford
Sleno R, Hbert TE (2018) Chapter five—the dynamics of GPCR oligomerization and their functional consequences. In: Arun KS, (ed) International review of cell and molecular biology, vol 338 of G protein-coupled receptors: emerging paradigms in activation, signaling and regulation Part A, pp 141–171. Academic Press
Smoluchowski M (1918) Versuch einer mathematischen Theorie der Koagulationskinetik kolloider Lösungen. Zeitschrift für Physikalische Chemie 92(1):129–168
Stephen S, Neil D (2018) Model reduction permits Turing instability analysis of arbitrary reaction–diffusion models. J R Soc Interface 15:213298
Stillwell W (2013) An introduction to biological membranes: from bilayers to rafts. Newnes, Amsterdam
Strogatz SH (1994) Nonlinear dynamics and chaos with applications to physics. Biology, chemistry and engineering, 1st edn. Westview Press, Routledge
Trong PK, Nicola EM, Goehring NW, Kumar KV, Grill SW (2014) Parameter-space topology of models for cell polarity. N J Phys 16(6):065009
Turing AM (1952) The chemical basis of morphogenesis. Philos Trans R Soc Lond Ser B Biol Sci 237(641):37–72

van Oosterom A (2006) The surface Laplacian operator of the potentials on a bounded volume conductor has a unique inverse. IEEE Trans Biomed Eng 53(7):1449–1450
Yanyan C, Javier B (2019) A non-linear analysis of Turing pattern formation. PLoS ONE 14(8):1–9
Yeagle L (2011) The structure of biological membranes. CRC Press, Boca Raton
Zhang Y-J, Shi J-M, Bai C-J, Wang H, Li H-Y, Yi W, Ji S-R (2012) Intra-membrane oligomerization and extra-membrane oligomerization of amyloid-β peptide are competing processes as a result of distinct patterns of motif interplay. J Biol Chem 287(1):748–756
Zidar M, Kuzman D, Ravnik M (2018) Characterisation of protein aggregation with the smoluchowski coagulation approach for use in biopharmaceuticals. Soft Matter 14(29):6001–6012

Publisher's Note Springer Nature remains neutral with regard to jurisdictional claims in published maps and institutional affiliations.

Affiliations

Lucas M. Stolerman[1] · Michael Getz[1] · Stefan G. Llewellyn Smith[1,2] · Michael Holst[3,4] · Padmini Rangamani[1]

1 Department of Mechanical and Aerospace Engineering, University of California, San Diego, La Jolla, CA 92093-0411, USA

2 Scripps Institution of Oceanography, University of California, San Diego, La Jolla, CA 92093-0213, USA

3 Department of Mathematics, University of California, San Diego, La Jolla, CA 92093-0112, USA

4 Department of Physics, University of California, San Diego, La Jolla, CA 92093-0424, USA